

Scaling laws for convection and jet speeds in the giant planets

ADAM P. SHOWMAN

University of Arizona, Tucson, AZ and Columbia University, New York, NY

YOHAI KASPI

California Institute of Technology

GLENN R. FLIERL

Massachusetts Institute of Technology

ABSTRACT

Three dimensional studies of convection in deep spherical shells have been used to test the hypothesis that the strong jet streams on Jupiter, Saturn, Uranus, and Neptune result from convection throughout the molecular envelopes. Due to computational limitations, these simulations must be performed at parameter settings far from Jovian values and generally adopt heat fluxes 5–10 orders of magnitude larger than the planetary values. Several numerical investigations have identified trends for how the mean jet speed varies with heat flux and viscosity, but no previous theories have been advanced to explain these trends. Here, we show using simple arguments that if convective release of potential energy pumps the jets and viscosity damps them, the mean jet speeds split into two regimes. When the convection is weakly nonlinear, the equilibrated jet speeds should scale approximately with F/ν , where F is the convective heat flux and ν is the viscosity. When the convection is strongly nonlinear, the jet speeds are faster and should scale approximately as $(F/\nu)^{1/2}$. We demonstrate how this regime shift can naturally result from a shift in the behavior of the jet-pumping efficiency with heat flux and viscosity. Moreover, both Boussinesq and anelastic simulations hint at the existence of a third regime where, at sufficiently high heat fluxes or sufficiently small viscosities, the jet speed becomes independent of the viscosity. We show based on mixing-length estimates that if such a regime exists, mean jet speeds should scale as heat flux to the 1/4 power. Our scalings provide a good match to the mean jet speeds obtained in previous Boussinesq and anelastic, three-dimensional simulations of convection within giant planets over a broad range of parameters. When extrapolated to the real heat fluxes, these scalings suggest that the mass-weighted jet speeds in the molecular envelopes of the giant planets are much weaker—by an order of magnitude or more—than the speeds measured at cloud level.

1. Introduction

At the cloud levels near ~ 1 bar pressure, numerous east-west (zonal) jet streams dominate the meteorology of the giant planets Jupiter, Saturn, Uranus, and Neptune, but the depth to which these jets extend into the interior remains unknown. Endpoint theoretical scenarios range from weather-layer models where the jets are confined to a layer several scale heights deep to models where the

Corresponding author address:

A.P. Showman, Department of Planetary Sciences, Lunar and Planetary Laboratory, University of Arizona, Tucson, AZ 85721 (showman@lpl.arizona.edu). Part of the work was completed while APS was on sabbatical at Columbia University, Department of Applied Physics and Applied Mathematics, New York, NY 10027.

jets extend throughout the molecular envelope ($\sim 10^4$ km thick) on cylinders parallel to the rotation axis (for a review see Vasavada and Showman 2005). For Jupiter, in-situ observations by the Galileo probe at 7°N latitude show that the equatorial jet extends to at least ~ 20 bars (~ 150 km below the visible clouds) (Atkinson et al. 1997), and indirect inferences suggest that the jets at other latitudes extend to at least ~ 5 – 10 bars pressure (e.g., Dowling 1995; Legarreta and Sánchez-Lavega 2008; Morales-Juberias and Dowling 2005; Sánchez-Lavega et al. 2008). At Neptune, gravity data suggest that the fast jets are confined to the outermost few percent of the planet’s mass (Hubbard et al. 1991). Comparable data are currently lacking for Jupiter and Saturn but will be obtained by NASA’s *Juno* and *Cassini* missions, respectively, in coming years.

Three-dimensional (3D) numerical simulations of convection in rotating spherical shells have been performed by several groups to investigate the possibility that the jets on the giant planets result from convection in the interior. Both free-slip and no-slip momentum boundary conditions at the inner and outer boundaries have been explored; of these, the free-slip case—which allows the development of strong zonal flows—is most relevant to giant planets. So far, such studies have neglected the high electrical conductivity and coupling to magnetic fields expected to occur in the deep ($\gtrsim 1$ Mbar) planetary interior.

In this line of inquiry, most studies to date make the Boussinesq assumption in which the basic-state density, thermal expansivity, and other background properties are assumed constant with planetary radius; the convection is driven by a constant temperature difference imposed between the bottom hot boundary and top cold boundary (Aurnou et al. 2008; Aurnou and Heimpel 2004; Aurnou and Olson 2001; Christensen 2001, 2002; Heimpel and Aurnou 2007; Heimpel et al. 2005). These studies show that convection with free-slip boundaries can drive multiple jets with speeds greatly exceeding the convective speeds. Studies using thick shells tend to produce ~ 3 – 5 jets (Aurnou and Olson 2001; Christensen 2001, 2002). When the shell thickness is only $\sim 10\%$ of the planetary radius, then at least under some parameter combinations, ~ 15 – 20 jets can occur, similar to the number observed on Jupiter and Saturn (Heimpel and Aurnou 2007; Heimpel et al. 2005). Nevertheless, many factors in addition to shell thickness can affect the number of jets.

In real giant planets, the density and thermal expansivity each vary by several orders of magnitude from the cloud layer to the deep interior, and a new generation of convection models is emerging to account for this strong radial variation in basic-state properties. Using the anelastic approximation, which accounts for this layering, Evonuk and Glatzmaier (2006, 2007), Evonuk

(2008) and Glatzmaier et al. (2009) present idealized two-dimensional (2D) simulations in the equatorial plane exploring hypothetical basic-state density profiles, with density varying by up to a factor of 55 across the convection zone. In contrast, Jones and Kuzanyan (2009) present 3D simulations using an idealized basic-state density structure, with density varying by a factor of up to 148, while Kaspi et al. (2009, 2010) present 3D simulations with a realistic Jovian interior structure, with density varying by nearly a factor of 10^4 from the deep interior to the 1-bar level. These anelastic studies likewise suggest that the jets could penetrate deeply through the molecular envelope.

A challenge with all of the above-described simulations is that, for computational reasons, they must be performed using heat fluxes and viscosities that differ greatly from those on Jupiter, Saturn, Uranus, and Neptune (Fig. 1). Thus, while simulations can produce jets with speeds similar to the observed values of ~ 100 – 200 m sec^{-1} for some combinations of parameters (e.g., Aurnou et al. 2007, 2008; Aurnou and Olson 2001; Christensen 2001, 2002; Heimpel and Aurnou 2007; Heimpel et al. 2005; Jones and Kuzanyan 2009; Kaspi et al. 2009), this does not imply that convection in the interior of real giant planets would necessarily produce jets with such speeds. In fact, depending on the parameter combinations, simulations with free-slip boundary conditions can produce jets that equilibrate to mean speeds¹ ranging over many orders of magnitude, from arbitrarily small (less than 1 m sec^{-1}) to 1000 m sec^{-1} or more. Assessing the likely wind speeds in the molecular envelopes of the real giant planets—and determining whether their observed jets can be pumped by convection in their interiors—requires the development of a theory that can be extrapolated from the simulation regime to the planetary regime.

Currently, however, there is no published theory that can explain the jet speeds obtained in simulations with free-slip boundaries nor their dependence on heat flux, viscosity, and other parameters. Several investigations have presented scaling laws describing how the mean zonal-wind speeds vary with control parameters when *no-slip* boundary conditions are used, as potentially relevant to Earth’s outer core (e.g., Aubert 2005; Aurnou et al. 2003). These are essentially theories for the magnitude of wind shear in the fluid interior for cases where the zonal velocity is pinned to zero at the boundaries. However, these scaling laws are not applicable to the giant planets, where the fluid at the outer boundary can move freely, lacks a frictional Ekman layer, and exhibits

¹Calculated in a suitably defined way, such as $\sqrt{2K/M}$, where K and M are the total kinetic energy and mass; this is essentially the mass-weighted characteristic wind speed of the fluid.

strong jets. Several attempts have also been made to quantify how the *convective* velocities scale with parameters, but—regardless of the boundary conditions—these relationships cannot be applied to the *jet* speeds because the convective and jet speeds can differ greatly and their ratio may depend on the heat flux and other parameters.

The goal of this paper, therefore, is to develop scaling laws for how the jet speeds depend on heat flux and viscosity that explain the simulated behavior within the simulated regime and, ideally, allow an extrapolation to real planets. The simulations themselves make a number of simplifications (e.g., ignoring magnetohydrodynamics in the deep interior at pressures exceeding ~ 1 Mbar), but in our view building a theory of this idealized case is a prerequisite for understanding more realistic systems.

We first quantify the degree of overforcing in current studies, since this issue has received little attention in the literature (Section 2). Next, we quantify the dependence of the convective speeds on planetary parameters and compare them to results from an anelastic general circulation model from Kaspi et al. (2009) (Section 3). Armed with this information, we construct simple scalings for the characteristic jet speeds in three regimes. In the first two regimes (Section 4), the viscosity is large enough so that viscous damping of the jets provides the dominant kinetic-energy loss mechanism. Christensen (2002) suggested the existence of a third regime where the jet speeds become independent of the viscosity; we construct possible scalings for this regime in Section 5. In Section 6, we combine the three regimes and discuss extrapolations to Jupiter. Section 7 concludes.

2. Degree of overforcing

For numerical reasons, current 3D simulations of convection in the giant planets must use viscosities many orders of magnitude larger than the molecular viscosities. This results from the coarse grid resolution in the models: to be numerically converged, such a model must have convective boundary layer and convective plume thicknesses of at least a gridpoint, and this requires very large viscosities. Given the enhanced damping of the kinetic energy implied by this constraint, such simulations can achieve wind speeds similar to those on the giant planets only by adopting heat fluxes orders of magnitude too large.

Moreover, even in the absence of such a viscous damping, enhanced heat fluxes are computationally necessary simply to achieve spin up within available integration times. To illustrate, imagine a giant planet that initially has no winds, and ask how long it would take to spin the zonal jets up to full strength if the jets penetrate through the molecular region (down to ~ 1 Mbar pressure on Jupiter and Saturn). This corresponds to a kinetic energy per area of $\sim u^2 \Delta p / g$, where u is the characteris-

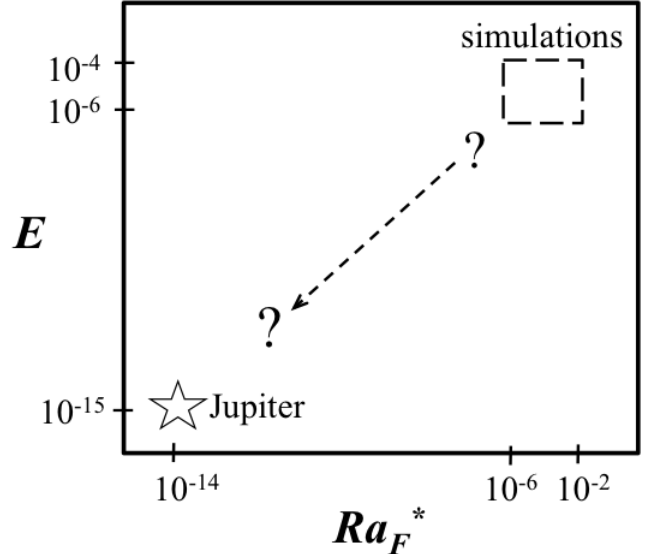


FIG. 1. Illustration of the parameter space associated with convection in rotating spherical shells. The modified-flux Rayleigh number Ra_F^* (abscissa) and Ekman number E (ordinate) can be viewed as non-dimensionalized heat flux and viscosity, respectively. The Prandtl number, giving the ratio of viscosity to thermal diffusivity, constitutes a third dimension. Published simulations access a small region of parameter space with values of Ra_F^* and E typically 10^{-6} or greater, but the actual values for Jupiter are $\sim 10^{-14}$ or less. It is unknown whether convection at Jupiter-like values of Ra_F^* and E would produce Jupiter-like wind speeds.

tic jet speed ($\sim 30 \text{ m sec}^{-1}$ on Jupiter), g is gravity, and $\Delta p \sim 1$ Mbar is the pressure thickness across which the jets are assumed to extend. On giant planets, the work to spin up the winds comes from the convection, driven by internal heat fluxes ranging from 0.3 W m^{-2} or less for Uranus and Neptune to 5 W m^{-2} for Jupiter. Given these small available fluxes, the characteristic pumping time of the jets is $\sim 10^5$ years. This is a lower limit, because it assumes that the efficiency of converting the heat flux into kinetic energy is close to 100%; in reality, the efficiency will be less, and much of the power produced will be used to resist frictional losses in the simulations. In contrast, published state-of-the-art high-resolution numerical simulations, if expressed in dimensional units, typically integrate months to years (e.g., Aurnou et al. 2008; Aurnou and Olson 2001; Christensen 2001, 2002; Heimpel and Aurnou 2007; Heimpel et al. 2005; Jones and Kuzanyan 2009; Kaspi et al. 2009). Thus, the heat fluxes must be enhanced by at least 3–5 orders of magnitude simply to allow the simulations to spin up within achievable integration times.

Most convection papers cast the equations in nondimensional form, rendering unclear the actual degree to

which these simulations are overforced. One can quantify the degree of overforcing as follows. In these simulations, the specified control parameters are the Rayleigh number Ra , the Ekman number E , and the Prandtl number Pr , defined as follows:

$$Ra = \frac{\alpha g \Delta T D^3}{\kappa \nu}, \quad E = \frac{\nu}{\Omega D^2}, \quad Pr = \frac{\nu}{\kappa} \quad (1)$$

where α , g , κ , and ν are the thermal expansivity, gravity, thermal diffusivity, and kinematic viscosity. D is the thickness of the convecting layer, ΔT is the imposed temperature drop across this layer, and Ω is the planetary rotation rate.

The heat flux, which is an output, is typically cast as a Nusselt number Nu , which gives the ratio of the total (convective plus conductive) heat flux to a reference conductive flux that would be conducted across a system with the same temperature drop and thickness:

$$Nu = \frac{F_{\text{tot}}}{F_{\text{cond}}} = \frac{DF_{\text{tot}}}{\kappa \rho c_p \Delta T}, \quad (2)$$

where F_{tot} is the total flux, the thermal conductivity is $\kappa \rho c_p$, and $F_{\text{cond}} = \kappa \rho c_p \Delta T / D$. At Rayleigh numbers far exceeding the critical value, the total heat flux approximately equals the convective heat flux.

So how may we determine the *dimensional* heat flux for a nondimensional simulation with specified Ra , E , Pr , and Nu ? Using (1) and (2) shows that

$$F_{\text{tot}} = \frac{\Omega^3 D^2 \rho c_p}{\alpha g} \frac{E^3 Ra Nu}{Pr^2}. \quad (3)$$

Because convection is driven by buoyancy associated with a heat flux, an alternate Rayleigh number, defined in terms of the heat flux rather than a temperature contrast, is useful:

$$Ra_F = \frac{\alpha g F_{\text{tot}} D^4}{\rho c_p \nu \kappa^2}. \quad (4)$$

Christensen (2002) argued that, in the limit of small diffusivities, the fluid behavior should become independent of the diffusivities, and he defined a modified heat-flux Rayleigh number that is independent of these diffusivities. This can be constructed by multiplying Eq. (4) by $E^3 Pr^{-2}$, giving²

$$Ra_F^* = \frac{\alpha g F_{\text{tot}}}{\rho c_p \Omega^3 D^2}. \quad (5)$$

In the limit of small diffusivities, one thus expects that the behavior should scale with Ra_F^* rather than Ra . Casting Eq. (5) as an expression for heat flux, we have

$$F_{\text{tot}} = \frac{\Omega^3 D^2 \rho c_p}{\alpha g} Ra_F^*. \quad (6)$$

For a giant planet, all the dimensional parameters in Eq. (6) are known. Consider Jovian values of $\Omega = 1.74 \times 10^{-4} \text{ sec}^{-1}$, $D \approx 2 \times 10^4 \text{ km}$, $c_p = 1.3 \times 10^4 \text{ J kg}^{-1} \text{ K}^{-1}$, and $g = 26 \text{ m sec}^{-2}$. For interpreting Boussinesq simulations in the context of giant planets, an ambiguity is that the thermal expansivity and density vary greatly from atmospheric values at the top to liquid values in the interior. Using atmospheric values corresponding to a pressure of ~ 100 bars, where the temperature is $\sim 600 \text{ K}$, we have $\rho \approx 4 \text{ kg m}^{-3}$ and $\alpha \approx 1.6 \times 10^{-3} \text{ K}^{-1}$. Considering the simulation in Christensen (2001), where $Pr = 1$, $E = 3 \times 10^{-5}$, $Ra = 10^8$, and $Nu \approx 10$, we then have heat fluxes of $\sim 10^5 \text{ W m}^{-2}$. However, given that the vast bulk of the interior behaves as a liquid, much more appropriate values are $\rho \sim 10^3 \text{ kg m}^{-3}$ and $\alpha \sim 10^{-5} \text{ K}^{-1}$, relevant to the bulk of Jupiter's interior. These values imply fluxes of $\sim 10^9\text{--}10^{10} \text{ W m}^{-2}$. Similar estimates imply that the simulations of Heimpel and Aurnou (2007) and Aurnou et al. (2008) adopt a heat flux of $\sim 10^8 \text{ W m}^{-2}$. Aurnou et al. (2007)'s simulations of Uranus and Neptune adopt a heat flux of $\sim 10^7 \text{ W m}^{-2}$.

Given the great variation of density and thermal expansivity with radius on a giant planet, future studies will increasingly adopt models that incorporate the full radial variation of these parameters. This will require extending the definition of Rayleigh number. We adopt the following definition, in which a mass-weighted average is performed over the radially varying quantities (Kaspi et al. 2009):

$$Ra_F^* = \frac{1}{\Omega^3 D^2} \langle \frac{\alpha g F_{\text{tot}}}{\rho c_p} \rangle, \quad (7)$$

where the mass-weighted average is defined as $\langle \dots \rangle = \int (\dots) \rho r^2 dr / \int \rho r^2 dr$.

Anelastic simulations that adopt realistic radial profiles for the density and thermal expansivity lack the ambiguity described above. Kaspi et al. (2009) force the flow not through a constant-temperature boundary condition but by introducing internal heating and cooling. Integrating their heating profile over the depth of the planet gives an effective heat flux with a maximum of $\sim 10^9 \text{ W m}^{-2}$ in the deep interior with values decaying to zero in the atmosphere. Similarly, Jones and Kuzanyan (2009) estimate a dimensional heat flux of $\sim 10^9 \text{ W m}^{-2}$ for their simulations, broadly consistent with the estimates made here.

The implication is that the simulations in Christensen (2001, 2002), Aurnou and Olson (2001), Heimpel and Au-

²Christensen (2002) made alternate definitions of Ra_F^* and Nu that included a non-dimensional factor of η (the ratio of the inner-to-outer radius adopted in the simulations) in the numerator of Eqs. 2 and 4. We forgo this factor here.

rnou (2007), Aurnou et al. (2008), Kaspi et al. (2009) and related studies are overforced by ~ 6 – 10 orders of magnitude. The overforcing compensates for the numerical need to use high diffusivities and achieve a steady state over reasonable time scales. In non-dimensional terms, the numerical models adopt Ra_F^* of 10^{-8} or greater while Jupiter’s Ra_F^* value is $\sim 10^{-14}$.

3. Convective velocities and buoyancies

In a giant planet, convection in the interior transports the interior heat flux. To order-of-magnitude, one thus expects that

$$F \sim \rho c_p w \delta T, \quad (8)$$

where F is the convected heat flux, w is the characteristic magnitude of the vertical convective velocity, and δT is the characteristic magnitude of the temperature difference between a convective plume and the surrounding fluid.

In a rapidly rotating, low-viscosity fluid, the scaling for convective velocities is typically written (e.g., Boubnov and Golitsyn 1990; Fernando et al. 1991; Golitsyn 1980, 1981; Stevenson 1979)³

$$w \sim \left(\frac{\alpha g F}{\rho c_p \Omega} \right)^{1/2}. \quad (9)$$

It is known that Eq. (9) provides a reasonable representation of convective velocities for laboratory experiments in rotating tanks (e.g., Boubnov and Golitsyn 1990; Fernando et al. 1991; Golitsyn 1981). Several authors have also suggested that Eq. (9) is relevant for the dynamo-generating regions of planetary interiors, where a three-way balance between buoyancy, Coriolis, and Lorentz forces is often assumed (e.g., Starchenko and Jones 2002; Stevenson 2003). To our knowledge, however, no broad assessment of its accuracy has been made for convection in the molecular interior of a giant planet. To do so, we performed three-dimensional numerical simulations of convection in Jupiter’s interior using an anelastic general circulation model based on the MITgcm (Kaspi et al. 2009). The radial dependence of gravity, basic-state density, compressibility, and thermal expansivity correspond to a realistic Jupiter interior structure calculated with the SCVH equation of state (Saumon et al. 1995). Simulations with a broad range of parameters were explored (Table 1). All of our simulations are in a rapidly rotating, low-viscosity regime, with geostrophic balance holding on large scales (see, e.g., Kaspi et al. 2009, Fig. 6).

³Equation (9) can be heuristically derived by assuming that the convective buoyancy force per mass, $g \alpha \delta T$, is balanced by the vertical Coriolis force due to the turbulent eddy motions, $\Omega u'$, where u' is the horizontal eddy velocity. Assuming that the turbulent eddy motions are approximately isotropic ($u' \sim w$) and invoking Eq. (8) then leads to Eq. (9).

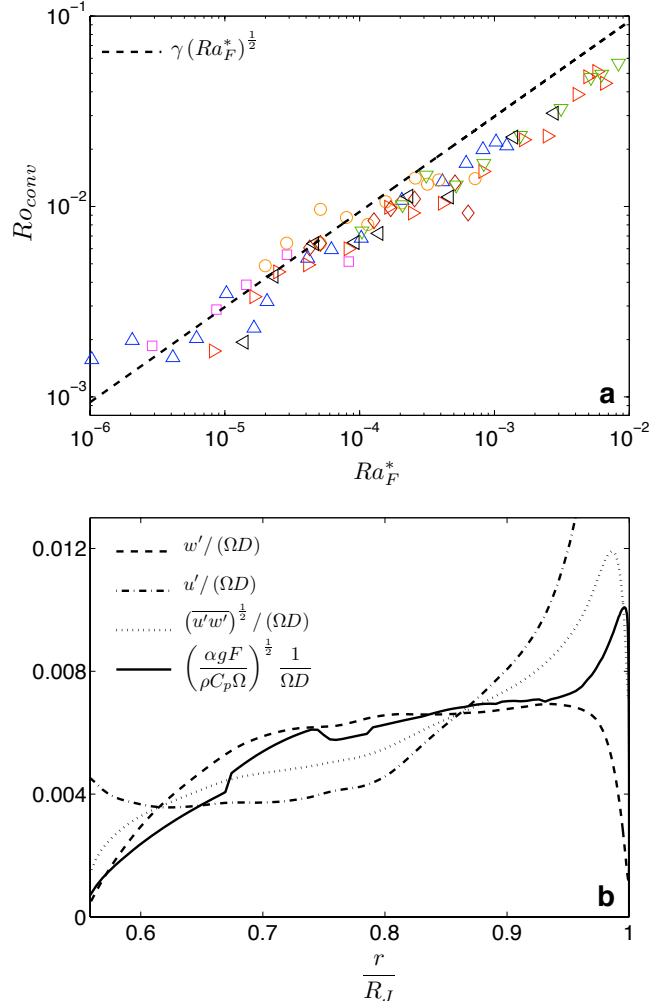


FIG. 2. *Top*: Mass-weighted convective vertical wind speed (calculated as the deviation of vertical wind speed from its zonal mean) versus modified heat-flux Rayleigh number for a range of anelastic simulations. The velocities are expressed as a convective Rossby number, defined as velocity divided by ΩD . Dashed line is the scaling of Eq. (10) with $\gamma = 1$. See Table 1 for definitions of the symbols. *Bottom*: Radial variation of the horizontally averaged velocity components for an anelastic simulation with parameters $Ra_F^* = 2.89 \times 10^{-5}$, $E = 1.5 \times 10^{-4}$, and $Pr = 10$. Depicts deviation of vertical velocity from its zonal mean (dashed), deviation of the zonal velocity from its zonal mean (dashed-dotted), the square root of their zonally averaged correlation $(\overline{u'w'})^{1/2}$ (dotted), and the scaling from Eq. (9) evaluated using the radially varying thermal expansivity α , basic-state density $\bar{\rho}$, heat flux F , and gravity. Note that all the anelastic simulations in this paper use the full Jovian interior structure with a factor of $\sim 10^4$ variation in density from top to bottom. For more details on the experiments see Kaspi (2008) and Kaspi et al. (2009).

	$E \times 10^4$	Pr	$Ra_F^* \times 10^5$	$Ro \times 10^3$	symbol	color
Boussinesq	0.3	10	0.052, 0.105, 0.157, 0.261, 0.523, 1.04, 2.09, 3.66, 5.23	1.07, 1.82, 3.15, 6.8, 6.33, 12.8, 21.8, 32.7, 41.1	square	black
Anelastic	1.5	10	0.289, 0.866, 1.44, 2.89, 8.31	2.47, 5.01, 7.43, 23, 15.1	square	magenta
	4	10	0.103, 0.206, 0.411, 0.617, 1.03, 1.64, 2.06, 4.11, 6.17, 10.3, 20.6, 41.1, 61.7, 82.2, 103, 123	0.671, 0.776, 1.38, 1.88, 3.82, 4.85, 5.46, 8.55, 13.8, 20.5, 34.5, 55.9, 69.8, 77.1, 84.7, 91.3	up-pointing triangle	blue
	6	10	1.39, 2.31, 4.63, 9.25, 13.9, 23.1, 46.3, 139, 278	2.78, 5.27, 6.8, 13.3, 18.9, 29.1, 48, 82.2, 107	left-pointing triangle	black
	8	10	0.822, 1.64, 2.47, 4.11, 8.22, 16.4, 24.7, 41.1, 82.2, 164, 247, 411, 493, 576, 658	1.27, 3.54, 5.18, 7.05, 12.6, 19.5, 25, 36.9, 57.7, 78.1, 93, 96.7, 109, 115, 108	right-pointing triangle	red
	9	10	10.4, 20.8, 31.2, 52, 83.3, 156, 312, 520, 624, 833	15.6, 19.4, 27.9, 44.9, 57.8, 71.4, 95.6, 113, 116, 114	down-pointing triangle	green
	2.5, 3, 4, 5, 6, 7, 8, 9, 10, 11, 15	10	1.99, 2.87, 5.11, 7.98, 11.5, 15.6, 20.4, 25.9, 31.9, 38.6, 71.8	5.47, 8.03, 16.2, 18.9, 21.4, 24.8, 25.8, 28, 31.3, 31.6, 41.2	circle	orange
	4	0.8, 1, 2, 3, 4, 10, 12	63.8, 51.1, 25.5, 17, 12.8, 5.11, 4.26	70.4, 74, 50.4, 39.5, 31.9, 16.2, 14	diamond	red
	9	1	31.2, 52, 104, 520	17.4, 44.8, 55.4, 123		
	1, 2, 2.5, 3, 3.5, 4, 4.5, 5, 5.5, 6, 6.5, 7, 8, 8.5, 10, 12	10	5.12	34.9, 27.9, 23.9, 18.6, 17, 16.2, 14.3, 13.2, 11.4, 12.7, 11.2, 10.1, 9.26, 9.39, 7.58, 10.6		
	2, 3, 5, 8, 15, 30	10	41.1	71, 59.9, 49.9, 38.8, 25.7, 17.4		

TABLE 1. List of numerical integrations, using the model of Kaspi et al. (2009), that are presented in this paper. Each row lists a sequence of simulations. Columns 2, 3, and 4 give the control parameters, and column 5 gives the global-mean, mass-weighted Rossby number. The last two columns give the symbol type and color used to present each sequence of simulations in Figs. 2, 5, and 8. All the anelastic model integrations in this paper adopt the full Jovian radial interior structure of gravity, density, thermal expansivity, compressibility, and other thermodynamic properties from Kaspi et al. (2009), corresponding to a factor of $\sim 10^4$ variation of density from top to bottom.

Our simulations show that Eq. (9) provides a good approximation over a wide range of heat fluxes and rotation rates. Figure 2 shows the mass-weighted mean convective velocities from the Kaspi et al. (2009) anelastic simulations (presented as a convective Rossby number, namely convective vertical velocity divided by ΩD) versus modified-flux Rayleigh number and compares it to Eq. (9). For the vast majority of simulations, the simulations differ less than a factor of ~ 3 from the scaling, indicating that Eq. (9) is quite accurate. This analysis complements Kaspi et al. (2009)'s finding that, within a specific simulation, Eq. (9) captures the approximate *radial dependence* of the convective velocity across the interior, over which α/ρ varies by a factor of $\sim 10^5$ (Fig. 2, *bottom*). Together, these results suggest that Eq. (9) is valid not only for the mass-weighted mean velocities but *locally* within the fluid.

Laboratory experiments suggest that a prefactor should exist on the right side of Eq. (9) with a value close to 2 (Boubnov and Golitsyn 1990; Fernando et al. 1991; Golitsyn 1981); however, our simulations are better matched when no prefactor is used.

We can nondimensionalize the convective velocities using a convective Rossby number, $Ro_{\text{conv}} \equiv w/(\Omega D)$. The convective flux, F , equals F_{tot} minus the conductive flux. The conductive flux is only important near the critical Rayleigh number, and in this limit it becomes F_{cond} from Section 2. Making the approximation that the conductive flux equals F_{cond} , Eq. (9) nondimensionalizes to yield

$$Ro_{\text{conv}} \sim \gamma(Ra_F^* - Ra_F^{\text{crit}})^{1/2}, \quad (10)$$

where Ra_F^{crit} is the critical modified flux Rayleigh number for the onset of convection. Thus, at the critical Rayleigh number, the expression properly predicts zero convective velocities, and at greatly supercritical Rayleigh numbers it predicts $Ro_{\text{conv}} \sim \gamma(Ra_F^*)^{1/2}$. We have introduced a dimensionless prefactor γ for generality, but consistent with Fig. 2, we will assume $\gamma = 1$ when performing numerical estimates.

Like Eq. (10), many of our subsequent scalings will depend on the difference between the actual and critical Rayleigh numbers. For notational brevity, we therefore define this difference as

$$Ra_F^{\Delta} \equiv Ra_F^* - Ra_F^{\text{crit}}. \quad (11)$$

Equations (8–9) imply that the fractional density associated with convective plumes should scale as

$$\alpha\delta T \sim \left(\frac{F\Omega\alpha}{\rho c_p g}\right)^{1/2}. \quad (12)$$

Aubert et al. (2001) proposed an alternate scaling for the convective velocities in the limit of negligible viscosities, $Ro_{\text{conv}} \sim (Ra_F^*)^{2/5}$. They performed rotating

laboratory experiments in liquid gallium and water, and showed that this expression provides a reasonable fit to the convective velocities inferred for their experiments. In the numerical simulations of Christensen (2002) and Christensen and Aubert (2006), the poloidal component of the velocity field (which includes the convective velocities) depends on the Ekman number, but at small Ekman number seems to be converging toward an asymptotic dependence that is reasonably well represented by this $2/5$ scaling (with a prefactor of 0.5). In our case, Eqs. (9)–(10) provides a slightly better fit to the convective velocities, although the $2/5$ scaling (with a prefactor) is also adequate. Conversely, overplotting Eqs. (9)–(10) against Christensen (2002)'s simulation data shows that they match essentially as well as the $2/5$ scaling.

4. Scaling for the jet speeds

a. Experimental data

Our goal is to understand the physical processes governing the global-mean jet speeds as a function of heat flux and viscosity (i.e., Rossby number as a function of Ekman and Rayleigh numbers) for low-viscosity, rapidly rotating convection in spherical shells. To characterize this functional dependence requires numerous (~ 100 or more) numerical integrations so that the available parameter space is adequately sampled. While it is numerically possible in three-dimensional simulations to reach Ekman numbers as low as $3\text{--}4 \times 10^{-6}$ (e.g., Aurnou et al. 2008; Heimpel and Aurnou 2007; Heimpel et al. 2005; Jones and Kuzanyan 2009), this requires intensive computation and precludes the exhaustive survey of parameter space required to develop scaling laws. Instead, our strategy is to adopt more modest Ekman numbers (extending to 10^{-4} to 10^{-5}), which ensure that the dynamics are still in the low-viscosity, rapidly rotating regime (with geostrophic balance holding on large scales) yet allow numerous simulations to be performed. Here we present over 100 simulations. In addition, we extensively use the dataset of Christensen (2002), who systematically characterized the global-mean Rossby numbers as a function of Ekman and Rayleigh numbers in Boussinesq simulations with Ekman numbers as low as 10^{-5} . Despite being far from Jovian parameter values, all the simulations we present are in the appropriate rapidly rotating, low-viscosity regime, with geostrophic balance holding at large scales.

These numerical experiments demonstrate that the mean jet speeds depend significantly on the control parameters Ra_F^* and E . Figure 3 depicts the global-mean, mass-weighted Rossby number $Ro \equiv U/(\Omega D)$, where D is the thickness of the model domain and U is the domain-mean, mass-weighted wind speed, as a function of the control parameters in the Boussinesq simulations from

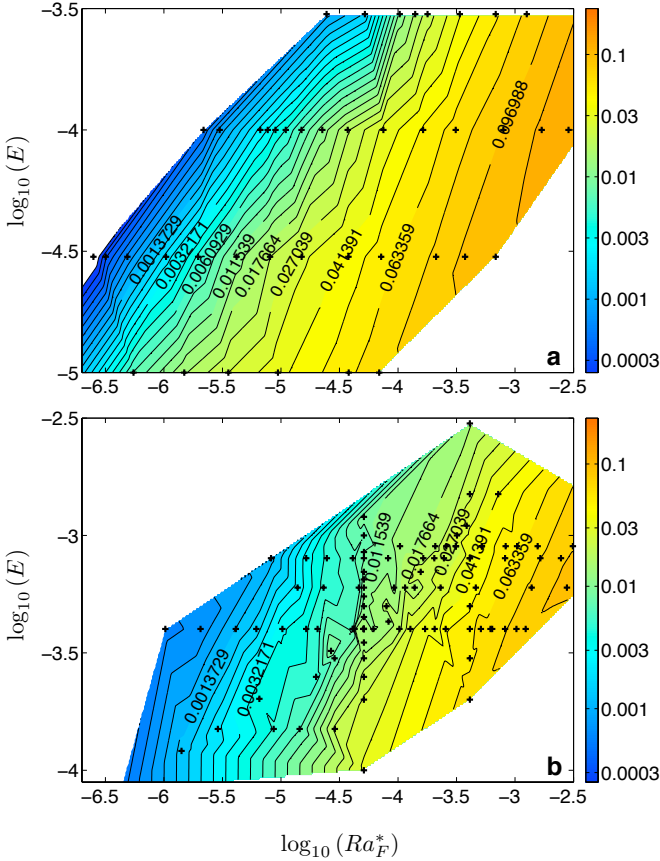


FIG. 3. Dependence of mass-weighted, domain-averaged jet speed on parameters from published simulations. Depicts the Rossby number (color and contours) as a function of modified flux Rayleigh number (abscissa) and Ekman number (ordinate) for Boussinesq simulations from Christensen (2002) (top) and anelastic simulations as described in Table 1 using the model of Kaspi et al. (2009) (bottom). Note that contours are evenly spaced in $\log(Ro)$ and that all figures in this paper use identical contour values and colorbars, facilitating intercomparison. In both panels, the pluses denote the locations of individual simulations. The range of Ekman numbers plotted is different in the two cases; anelastic cases are computationally more demanding and hence were run at larger Ekman numbers than the Boussinesq cases. The small-scale structure results from interpolation onto a fine grid of the coarsely spaced experimental points and may not be robust. The robust feature is the overall trend of positive slopes of constant- Ro contours, with mean slopes close to one, and Ro values ranging from ~ 0.1 on the right to ~ 0.0001 on the left. Note that, in both sets of simulations, the contours are widely spaced at Rossby numbers exceeding ~ 0.02 (right side of plot) but become tightly spaced at Rossby numbers less than ~ 0.02 (left side of plot), suggesting a regime transition.

Christensen (2002) (top panel) and the anelastic simulations described in Table 1 using the model of Kaspi et al. (2009) (bottom panel). The domain-averaged jet speeds range across three orders of magnitude even within the limited parameter space explored in these models, with some parameter combinations producing Jupiter-like speeds and others not. Rossby numbers range from ~ 0.0001 to 0.1 , corresponding to domain-mean wind speeds of ~ 1 to 1000 m sec^{-1} . In both cases, larger Ra_F^* and smaller E promote faster wind speeds. This makes sense qualitatively because, for a given rotation rate and planetary size, larger Ra_F^* implies larger heat flux (i.e., stronger forcing of the flow), while smaller E implies smaller viscosity (i.e., weaker damping of the flow). Kaspi et al. (2009) found that constant-wind-speed contours exhibit a slope (in the $\log(Ra_F^*)$ – $\log(E)$ diagram) of approximately $5/4$. The data from Christensen (2002) plotted in Fig. 3 likewise indicate that the wind-speed contours in his case exhibit a mean slope of approximately 1. For both sets of simulations, Fig. 3 also shows that the contours tend to be widely spaced toward the right and tightly spaced toward the left, with an approximate transition at $Ro \approx 0.02$. This suggests a transition between two regimes.

The processes that determine how mean jet speeds depend on Ra_F^* and E are not understood, however, and so the trends in Fig. 3 remain unexplained. Developing such an understanding is important because rotating spherical-shell convection is an inherently interesting physics problem, and also because extrapolation into the jovian parameter regime can only be performed once a theory for the Ra_F^* and E -dependence of the mean jet speeds has been developed. In the absence of such a theory, it is unknown whether convection at Jupiter-like values of Ra_F^* and E would generate Jupiter-like jet speeds. Explaining Fig. 3 is the core goal of this paper.

b. Regime I: Strongly nonlinear regime

Here, we construct a simple scaling theory based on energetic arguments to attempt an explanation for the jet speeds in the regime of fast jets ($Ro \gtrsim 0.02$ in Fig. 3, corresponding to jet speeds exceeding $\sim 100 \text{ m sec}^{-1}$), which we call Regime I.

First consider the forcing. A convecting fluid parcel traveling at a vertical speed w releases potential energy per mass at a rate $\dot{P} \sim gw\delta\rho/\rho$, where ρ is density and $\delta\rho$ is the magnitude of the density contrast between plumes and the background environment. Using the equation of state $\delta\rho = \alpha\rho\delta T$, where ρ represents a background density and δT is the magnitude of the temperature contrast between plumes and the background environment, we can write $\dot{P} \sim gw\alpha\delta T$. This potential energy is primarily converted into convective kinetic energy. Some

fraction ϵ of this energy is used to pump the zonal jets; we provisionally assume ϵ is constant but return to this assumption in Section 4c. Integrating over the planetary mass, the total power (in W) pumped into the jets is then approximately

$$\dot{P}_{\text{tot}} \sim 4\pi\epsilon \int \alpha\delta T g w \rho r^2 dr, \quad (13)$$

where the mass of an infinitesimal spherical shell of radial thickness dr is $4\pi\rho r^2 dr$. Both δT and w are *a priori* unknown, but they are related by the fact that convection transports the planet's interior heat flux (Eq. 8), which implies that $w\delta T \sim F/(\rho c_p)$. Thus, the power available to pump the jets can be written

$$\dot{P}_{\text{tot}} \sim 4\pi\epsilon \int \frac{\alpha g F}{c_p} r^2 dr. \quad (14)$$

Energy loss occurs through friction, which we assume acts as a diffusive damping of the winds with a viscosity ν (for the simulations, this would be the model viscosity that enters the definition of the Rayleigh and Ekman number; see Eq. 1). The power per mass dissipated by viscosity is approximately $\nu\nabla^2 u^2 \sim \nu k^2 u^2$, where k is the wavenumber of the structures dominating the dissipation, that is, the dominant wavenumber of $\nabla^2 u^2$. This implies a total rate of kinetic energy loss given by

$$\dot{K}_{\text{loss}} \sim 4\pi \int \nu k^2 u^2 \rho r^2 dr. \quad (15)$$

Now we equate energy gain (Eq. 14) and loss (Eq. 15) to obtain an expression for mean jet speed. In the case of a Boussinesq fluid, we note that α and ρ are constants and that F , g , c_p , and u are approximately constant (within a factor of ~ 3) and can be pulled out of the integral, yielding⁴

$$u \sim k^{-1} \left(\frac{\alpha g \epsilon F}{\rho c_p \nu} \right)^{1/2} \quad (16)$$

The case of an anelastic fluid is complicated by the large variation of α and ρ with radius, and even u may vary significantly from the top to the bottom of the domain (Kaspi et al. 2009). However, in the Kaspi et al. (2009) simulations, the mean jet speeds are relatively constant (within a factor of ~ 3) throughout most of the domain; only the top few % of the fluid mass experiences significant wind shear along the Taylor columns. To obtain a crude expression for the mass-weighted mean jet speed in the molecular region, we therefore assume that u is constant, allowing us to write:

$$u \sim k^{-1} \left(\frac{\epsilon}{\nu} \right)^{1/2} \left[\frac{\int \frac{\alpha g F}{\rho c_p} \rho r^2 dr}{\int \rho r^2 dr} \right]^{1/2}. \quad (17)$$

⁴A similar equation was derived, albeit with different arguments, by Ingersoll and Pollard (1982, Eq. 20).

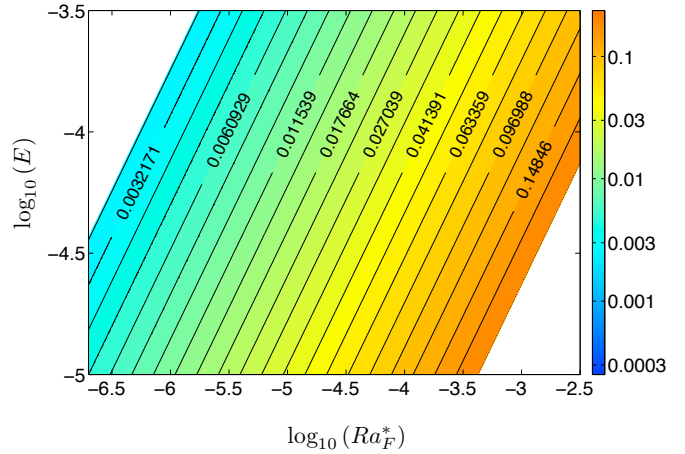


FIG. 4. Prediction of the scaling law for Regime I given in Eq. (18), in which the jet-pumping efficiency ϵ is assumed constant. Depicts contours of Rossby number versus modified flux Rayleigh number (abscissa) and Ekman number (ordinate). Adopts $kD = 5\pi$ and $\epsilon = 0.3$ (see text). Note the similarity of the slopes and values of the contours with the simulation results plotted in Fig. 3, particularly for Rossby numbers greater than ~ 0.02 .

Let us nondimensionalize these expressions so that they may be compared with the simulation results shown in Fig. 3. For both cases, we use $Ro \equiv u/(\Omega D)$ and the definition of E given in Eq. (1). Using the appropriate definition of the modified flux Rayleigh number yields the same nondimensional expression for both the Boussinesq and anelastic cases. Again approximating the convective flux F as the total flux minus F_{cond} , we obtain

$$Ro \approx \frac{\epsilon^{1/2}}{kD} \left(\frac{Ra_F^\Delta}{E} \right)^{1/2}, \quad (18)$$

where $Ra_F^\Delta \equiv Ra_F^* - Ra_F^{\text{crit}}$ (see Eq. 11). In Eq. (18), Ra_F^* is given by Eq. (5) for the Boussinesq case and by Eq. (7) for the anelastic case. Note that, in the highly supercritical regime in which we expect Eq. (18) to be valid, the critical Rayleigh number is generally negligible, so that Ra_F^Δ approximately equals Ra_F^* .

Thus, this simple theory predicts that the characteristic jet speed is proportional to $(F/\nu)^{1/2}$, or equivalently that the characteristic Rossby number is approximately proportional to $(Ra_F^*/E)^{1/2}$. Increases or decreases in Ra_F^* and E by the same factor leave Ro unchanged; in other words, this theory predicts that constant- Ro contours should have a slope of one in the Ra_F^*-E plane. This explains the fact that the empirically determined slopes in the simulations are close to one (see Fig. 3). In our theory, this behavior occurs because the forcing depends on the flux in the same way as damping depends on viscosity (namely, linearly). Thus, equal increases (or

decreases) in the flux and the viscosity cause alterations to the forcing and damping that cancel out, leading to a mean jet speed that is unchanged.

To further compare the theory to the simulations, Fig. 4 plots our solution (Eq. 18) as contours of Rossby number versus Ra_F^* and E . A choice of kD is necessary to evaluate Eq. (18). Kaspi et al. (2009)'s simulations show that, although the jets themselves are broad (with widths comparable to the domain thickness), the *curvature* of the wind $\nabla^2 u$, and thus the dissipation, exhibits a dominant wavelength of about $D/5$ (see their Fig. 10d). High-wavenumber structure in the flow shear also occurs in Christensen (2002)'s simulations. To account for this high-wavenumber structure, we adopt $kD \approx 5\pi$, and we calculate Fig. 4 using this value and $\epsilon = 0.3$.

Figure 4 reiterates the approximate agreements in the slopes of constant- Ro contours (compare Fig. 4 with Fig. 3). Moreover, the Ro values themselves also agree well, particularly in the regime of fast zonal jets where $Ro \gtrsim 0.02$. Throughout this part of the parameter space, the predicted Rossby number (Fig. 4) matches those obtained in the simulations (Fig. 3) to within a factor of ~ 2 at a given Ra_F^* and E , although the discrepancy approaches an order of magnitude toward the left side of the plot (at $Ro \lesssim 0.02$) where the simulated Rossby numbers seem to undergo a regime shift that is not captured by Eq. (18). Such a shift could result for example from a dependence of ϵ or k on Ra_F^* and E , a possibility not considered up to now. We return to this point in the next two subsections.

c. Regime II: Weakly nonlinear regime

For sufficiently small values of Ra_F^* , both the Boussinesq and anelastic simulations shown in Fig. 3 exhibit a regime shift where the dependence of Rossby number on Ra_F^* and E becomes steeper than the $(Ra_F^*/E)^{1/2}$ dependence discussed in the previous subsection. As Fig. 3 shows, at Rossby numbers smaller than ~ 0.01 – 0.02 , the constant- Ro contours become closely spaced, with a spacing indicating that a scaling $(Ra_F^*/E)^\xi$ with $\xi \approx 1$ might provide an approximate fit. There is also an indication that the slopes of the constant- Ro contours decrease toward the left side of the plot, particularly for Christensen's simulations.

These stronger dependences of Rossby number on Ra_F^* suggest a regime shift where different processes set the characteristic Rossby number at low Rossby number than at high Rossby number. In the strongly nonlinear regime explored in the previous subsection, the Rayleigh number is strongly supercritical, and the convection is chaotic and nonlinear. At lower Rayleigh numbers, when the Rayleigh number is only modestly greater than the critical value for convection, the convection is laminar and

more spatially organized. Here, we explore how this transition in convective behavior might lead to the regime shift in the jet speeds seen in Fig. 3.

To do so, we consider an alternate approach based the zonal momentum balance. Consider a cylindrical coordinate system whose axis aligns with the rotation axis, with coordinates (s, λ, z) corresponding to cylindrical radius (i.e., distance from the rotation axis), longitude, and distance above or below the equatorial plane, respectively. The zonal-mean zonal momentum equation then reads (cf Kaspi et al. 2009)

$$\frac{\partial \bar{u}}{\partial t} + 2\Omega \bar{v}_s + \frac{1}{\bar{\rho}} \nabla \cdot (\bar{\rho} \bar{u} \bar{\mathbf{v}}) + \frac{1}{\bar{\rho}} \nabla \cdot (\bar{\rho} \overline{u' \mathbf{v}'}) = \nu \nabla^2 \bar{u} \quad (19)$$

where u is the zonal wind, v_s is the cylindrically radial wind component (that is, the velocity component away from the rotation axis), overbars denote zonal means, primes deviations therefrom, and $\bar{\rho}$ is the mean density (constant in the Boussinesq case and a specified function of radius in the anelastic case). On the left side, the second term is the Coriolis acceleration. The third term represents advection due to the mean-meridional flow, and the fourth term represents the acceleration caused by eddies (i.e., Reynolds stress convergences). Generally speaking, for the geostrophic jovian regime, the Reynolds stress term dominates over the advection term (e.g. Kaspi et al. 2009).

We now average the equation in z (i.e. along the direction of Taylor columns). The Coriolis accelerations cancel out, because mass continuity prohibits any net, column-averaged motion toward or away from the rotation axis. Coupled with the free-slip boundary conditions and symmetry of the zonal-wind structure about the equatorial plane, the z -averaging also removes the z -components of the divergence and Laplacian terms. Neglecting the mean-flow advection terms, the column-averaged, steady-state balance becomes

$$\frac{1}{s^2 \bar{\rho}} \frac{\partial}{\partial s} (s^2 \overline{u' v'_s \bar{\rho}}) \approx \nu \frac{\partial}{\partial s} \left[\frac{1}{s} \frac{\partial}{\partial s} (s \bar{u}) \right] \quad (20)$$

which states that, in steady state, viscous drag associated with shear of the mean zonal wind $\partial \bar{u} / \partial s$ balances jet acceleration caused by eddies. Balances analogous to this expression have been written, for example, by Busse and Hood (1982), Busse (1983a), Busse (1983b), and Cardin and Olson (1994).⁵

We here use this balance to achieve a simple expression for the jet speeds. Approximate the left-hand side as $k \overline{u' v'_s}$, where k is the wavenumber (in cylindrical radius) over which $\overline{u' v'_s}$ varies significantly. Furthermore,

⁵An analogous balance was considered by Aubert et al. (2001) and Aubert (2005) but for the no-slip boundary condition where boundary-layer friction plays the dominant role in the damping.

suppose that *both* u' and v'_s scale like our expected convective velocity scale, so that $\overline{u'v'_s} \sim Cw^2$, where w is the convective velocity (e.g., from Eq. 9) and C is a correlation coefficient equal to one when u' and v'_s are perfectly correlated (i.e. when eastward u' always occurs with outward v'_s and vice versa) and equal to zero when u' and v'_s exhibit no correlation. We approximate the right-hand side as $\nu k^2 u$. The momentum balance then becomes

$$u \sim C \frac{w^2}{\nu k} \quad (21)$$

Nondimensionalizing, the Rossby number associated with the jets is

$$Ro \sim \frac{C}{kD} \frac{Ro_{\text{conv}}^2}{E} \quad (22)$$

An equation analogous to this was derived by Christensen (2002, his Eq. 3.12). Inserting our expression for the convective velocities (Eq. 10) yields

$$Ro \sim \frac{C\gamma^2}{kD} \frac{Ra_F^{\Delta}}{E}. \quad (23)$$

Thus, this theory predicts that, if the degree of correlation between u' and v'_s is independent of the control parameters (i.e., if C is constant), then the domain-mean jet speed scales as the convective flux over the viscosity, or equivalently the mean Rossby number scales as $(Ra_F^* - Ra_F^{\text{crit}})/E$. Away from the critical Rayleigh number, increases or decreases in Ra_F^* and E by the same factor leave Ro unchanged; therefore, as with the theory presented in the previous subsection, Eq. (23) predicts that constant- Ro contours should have slopes close to one in the logarithmic Ra_F^*-E plane. Near the critical Rayleigh number, however, the predicted slopes differ from one. If the critical modified flux Rayleigh number depends on E to a positive power less than one, then the constant- Ro contours increase in slope, becoming more vertical; if, however, Ra_F^{crit} depends on E to a power greater than one, then the constant- Ro contours decrease in slope, becoming more horizontal.

To evaluate Eq. (23) quantitatively, we require an expression for Ra_F^{crit} . By performing many simulations, Christensen (2002) determined empirically the critical Rayleigh number for each Ekman number he explored.⁶ Cardin and Olson (1994) performed a linear instability analysis of rotating convection in a spherical shell and found that, at $E \ll 1$, the critical value

⁶Christensen found that the critical values of a modified Rayleigh number $Ra^* \equiv RaE^2Pr^{-1}$ are 0.001005, 0.002413, 0.006510, and 0.016790 for Ekman numbers of 10^{-5} , 3×10^{-5} , 10^{-4} , and 3×10^{-4} , respectively. This is equivalent to modified flux critical Rayleigh numbers, Ra_F^{crit} , of 1.005×10^{-8} , 7.2×10^{-8} , 6.5×10^{-7} , and 5.04×10^{-6} for those same Ekman numbers, respectively. Equation (24) gives values that agree with these to within $\sim 10\%$.

of the ordinary Rayleigh number is a constant times $E^{-17/15}Pr^{4/3}(1+Pr)^{-4/3}$. Using the relationships between Ra and Ra_F^* (see Section 2), and noting that the Nusselt number equals one at the onset of convection, shows that the critical modified flux Rayleigh number should then scale as $E^{28/15}Pr^{-2/3}(1+Pr)^{-4/3}$. Most of Christensen's simulations adopt a Prandtl number of one and we find that his empirically determined critical Rayleigh numbers are well matched by the expression⁷

$$Ra_F^{\text{crit}} \approx 20E^{28/15}. \quad (24)$$

Given this dependence, contours of constant Rossby number in the logarithmic Ra_F^*-E plane should decrease in slope as one approaches the critical Rayleigh number (i.e., as one moves toward lower Ra_F^* values). This is qualitatively consistent with the behavior exhibited by Christensen's simulations (see Fig. 3).

d. Combining Regimes I and II

We have discussed two distinct regimes: (i) a regime of fast zonal winds and strongly supercritical convection where the simulated jet speeds seem well explained by the assumption that ϵ is constant (Regime I), and (ii) a regime of slow zonal winds and weakly supercritical convection where the jet speeds are approximately explained by the assumption that the correlation between the u' and v'_s velocity components is strong and roughly constant (Regime II). These led to two distinct scalings for the jet speeds: Eqs. (18) and (23) for the two regimes, respectively. Two issues now arise: First, how do we combine these regimes? Second, why should energetics and momentum considerations lead to different scalings? Both approaches should, in principle, yield the same answer within any given regime.

The resolution to both issues lies in the dependence of the correlation coefficient C and the convective jet-pumping efficiency ϵ on the control parameters. Consider, for example, the correlation coefficient. When the Rayleigh number is weakly supercritical and the flow is geostrophic, the convection forms broad, laminar convection rolls, which in a sphere become tilted in the prograde direction (Busse 1983a, b, 2002; Busse and Hood 1982; Christensen 2002; Kaspi 2008; Sun et al. 1993; Tilgner and Busse 1997, and others). This leads to highly correlated velocity components u' and v'_s , as illustrated in Fig. 5 (*top left*): ascending fluid parcels move prograde

⁷Dormy et al. (2004) found theoretically that the critical Rayleigh number should scale as $E^{-4/3}$ at low Ekman number, which would imply that Ra_F^{crit} should scale as $E^{5/3}$. However, this scaling does not fit Christensen's empirically determined critical Rayleigh numbers as well as Eq. (24), so we retain scaling (24) for the purposes of this paper. The choice has a negligible influence on our results.

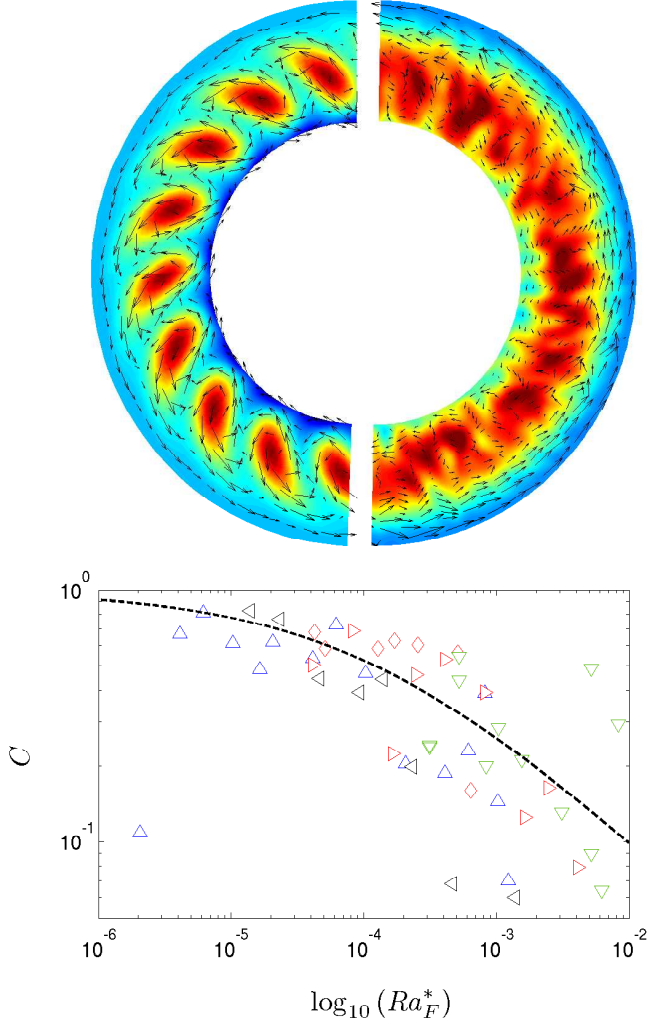


FIG. 5. *Top*: Snapshots in the equatorial plane of two anelastic, 3D simulations from Kaspi (2008) illustrating how the correlation between the convective velocity components depends on the supercriticality. Each slice shows half of the equatorial plane of one simulation (note however that the simulations each span 360° of longitude). Color depicts streamfunction and arrows denote velocity component in the equatorial plane. The left simulation is weakly supercritical; the strong correlation between outward and eastward velocity components is obvious. The right simulation is strongly supercritical; the correlation between the outward and eastward velocity components is weaker because of the complex, turbulent convective structure. *Bottom*: Depicts correlation coefficient C versus Ra_F^* for a range of anelastic simulations⁸. As expected qualitatively from the top panels, C decreases with Ra_F^* . Symbols are defined in Table 1.

while descending parcels move retrograde. As a result, at weakly supercritical Rayleigh numbers, the correlation coefficient C should be close to one, at least outside the tangent cylinder. On the other hand, when the convection is strongly supercritical, the convective structure is chaotically time-dependent and spatially complex; the velocity components u' and v'_s are positively correlated in some regions but negatively correlated in others. This is illustrated in Fig. 5 (*top right*). The net correlation is usually still positive, but the large degree of cancellation implies that, at strongly supercritical Rayleigh numbers, the correlation coefficient should drop significantly below one (Christensen 2002). As a result, one expects the correlation coefficient C to vary slowly with Ra_F^* near the critical Rayleigh number but to decrease more rapidly with increasing Ra_F^* at sufficiently supercritical Rayleigh numbers. This behavior can be seen in correlation coefficients calculated for a range of simulations versus Ra_F^* (Fig. 5, *bottom*).

Next consider the jet-pumping efficiency ϵ . The scaling (18), wherein the Rossby number scales with $(Ra_F^*/E)^{1/2}$, assumes that ϵ is constant. While this assumption seems to work well at sufficiently supercritical Rayleigh numbers, it *must* fail in the weakly supercritical regime where u' and v'_s are highly correlated. This is because, in this weakly nonlinear regime, the mean jet speeds scale quadratically with the convective velocities, and the power exerted to pump the jets scales as the Reynolds stresses times the jet speeds, namely as the fourth power of the convective velocities. The dependence of this quantity on the heat flux differs from the dependence of the convective potential-energy release on the heat flux. Since ϵ is the ratio of these quantities, ϵ cannot be constant in this regime.

A regime shift analogous to that seen for the jet speeds in Fig. 3—where Rossby numbers scale approximately with Ra_F^*/E at low Rossby number and approximately as $(Ra_F^*/E)^{1/2}$ at high Rossby number—can occur if the correlation coefficient depends weakly on Ra_F^* at low Ra_F^* yet strongly on Ra_F^* at high Ra_F^* . Likewise, it can occur if the jet-pumping efficiency depends strongly on Ra_F^* at low Ra_F^* yet weakly at high Ra_F^* .

To quantify these arguments, let us relate ϵ and C to each other. By definition, the efficiency ϵ is the ratio of work done to pump the jets to the work made available by convection:

$$\epsilon \sim \frac{\bar{u} \frac{1}{\bar{\rho}} \nabla \cdot (\bar{\rho} u' \mathbf{v}')}{g \omega \alpha \delta T}, \quad (25)$$

where it is understood that both the numerator and the denominator represent global averages. Expressing the numerator as $C k w^2$, the denominator as $g \alpha F / \rho c_p$ (using

Eq. 8), and non-dimensionalizing, we obtain

$$\epsilon \sim \frac{RoCkDRo_{\text{conv}}^2}{Ra_F^\Delta}. \quad (26)$$

Using Eq. (22) for the Rossby number yields the expression

$$\epsilon \sim C^2 \frac{Ro_{\text{conv}}^4}{ERa_F^\Delta}. \quad (27)$$

If we adopt $Ro_{\text{conv}} \approx \gamma(Ra_F^\Delta)^{1/2}$ for concreteness, we obtain finally

$$\epsilon \sim C^2 \gamma^4 \frac{Ra_F^\Delta}{E}. \quad (28)$$

Therefore, ϵ and C cannot simultaneously be constant when Ra_F^* or E are varied. Holding one constant requires the other to become a function of Ra_F^* and E .

Let us now make the simplest possible assumption regarding this regime shift—we postulate a regime with $C \approx \text{constant} = 1$ at low Rayleigh number and a regime with $\epsilon \approx \text{constant} \equiv \epsilon_{\text{max}}$ at high Rayleigh number. Quantitatively, there is no rigorous expectation that C or ϵ need be constant, nor (as described previously) is this assumption actually necessary for a regime shift to occur. Nevertheless, C and ϵ have upper limits of 1, so if some process causes them to increase with increasing (or decreasing) Ra_F^* , they might naturally plateau—at least over some range of parameter space—upon approaching their upper limits. Still, future theoretical work on what sets the Ra_F^* - and E -dependence of the correlation coefficient and jet-pumping efficiency is warranted.

Given these postulates, Eq. (28) implies that

$$C = \begin{cases} 1, & Ra_F^\Delta \lesssim \epsilon_{\text{max}} \gamma^{-4} E; \\ \epsilon_{\text{max}}^{1/2} \gamma^{-2} \left(\frac{E}{Ra_F^\Delta}\right)^{1/2}, & Ra_F^\Delta \gtrsim \epsilon_{\text{max}} \gamma^{-4} E \end{cases} \quad (29)$$

and

$$\epsilon = \begin{cases} \gamma^4 \frac{Ra_F^\Delta}{E}, & Ra_F^\Delta \lesssim \epsilon_{\text{max}} \gamma^{-4} E; \\ \epsilon_{\text{max}}, & Ra_F^\Delta \gtrsim \epsilon_{\text{max}} \gamma^{-4} E \end{cases} \quad (30)$$

To smoothly transition between the regimes, we adopt the expression

$$C \sim \left[1 + \frac{\gamma^2}{\epsilon_{\text{max}}^{1/2}} \left(\frac{Ra_F^\Delta}{E}\right)^{1/2} \right]^{-1} \quad (31)$$

which is merely the inverse of one over the value of C from the first regime plus one over the value of C from the second regime. This gives behavior equivalent to Eq. (29) in the two limits with a smooth transition in between. Given this expression, ϵ can then be evaluated from Eq. (28), yielding

$$\epsilon \sim \gamma^4 \left[1 + \frac{\gamma^2}{\epsilon_{\text{max}}^{1/2}} \left(\frac{Ra_F^\Delta}{E}\right)^{1/2} \right]^{-2} \frac{Ra_F^\Delta}{E}. \quad (32)$$

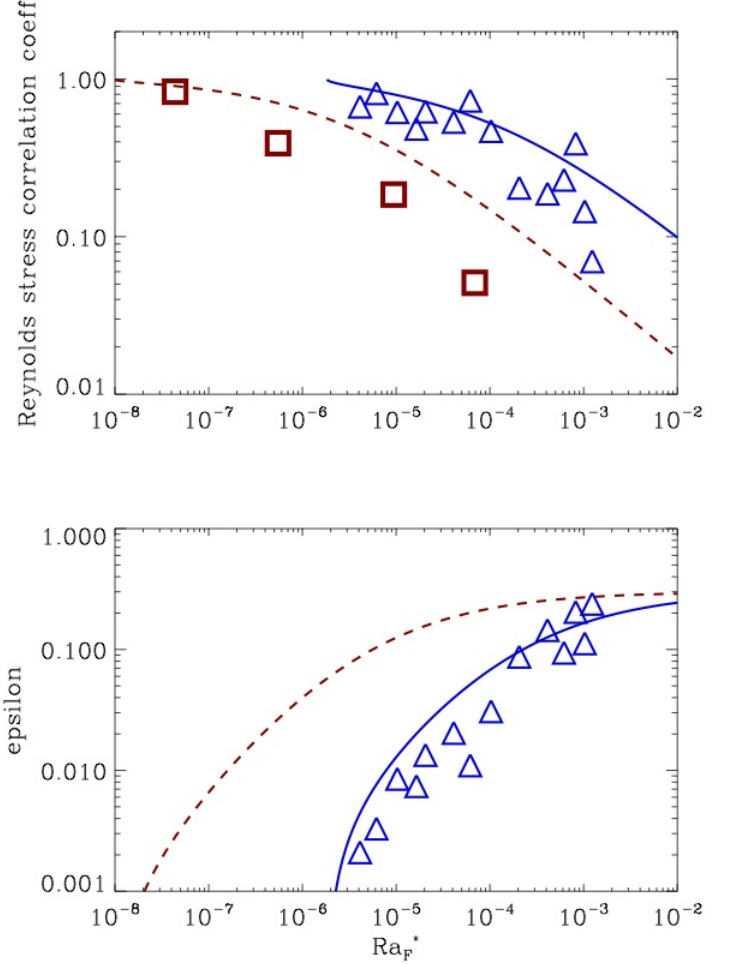


FIG. 6. *Top*: The correlation coefficient C , the ratio between the Reynolds stress $\overline{u'v'_s}$ and the product of the root-mean-square velocity magnitudes. *Bottom*: ϵ , the fraction of potential energy released by convection that is used to pump the jets. Blue triangles depict values we calculated rigorously from anelastic simulations at $E = 4 \times 10^{-4}$, while red squares denote values Christensen (2002) calculated rigorously from Boussinesq simulations at $E = 10^{-5}$. In both cases, values represent flow behavior outside the tangent cylinder. Curves plot Eqs. (31)–(32) at an Ekman number of 4×10^{-4} (solid blue) and 10^{-5} (dashed red) assuming $\gamma = 1$ and $\epsilon_{\text{max}} = 0.3$, with Ra_F^{crit} evaluated using $20E^{28/15}$ for the Boussinesq simulations and $0.4E^{28/15}$ for the anelastic simulations (the difference resulting from the differing Prandtl numbers; see Table 1).

Figure 6 plots ϵ and C versus Ra_F^* from available data and compares them to Eqs. (31)–(32). In particular, the blue triangles denote values of C and ϵ that we rigorously computed⁸ from the three-dimensional convective velocity and entropy fields for a sequence of anelastic simulations with $E = 4 \times 10^{-4}$. Additionally, the red circles denote values of C rigorously calculated by Christensen (2002) for a sequence of his simulations at $E = 10^{-5}$ (see his Table 3; note that no data on ϵ are available for Christensen’s simulations.) Blue and red solid curves denote the predictions of Eqs. (31)–(32) for $E = 4 \times 10^{-4}$ and 10^{-5} , respectively, and can be directly compared to the symbols of the same color.

Key points are as follows. First, the data indicate that, for both sets of simulations, C decreases with Ra_F^* , while ϵ increases with Ra_F^* . Second, and more importantly, the *slopes* of the trends change across the range of Ra_F^* explored. The trends of C in both sets of simulations depend relatively weakly on Ra_F^* toward the left but seem to steepen toward the right. For example, Christensen’s data indicate that a factor-of-two change in Ra_F^* cause a 1.28-fold change in C at low Ra_F^* but a 2.7-fold change in C at high Ra_F^* . Conversely, the data suggest that ϵ depends on Ra_F^* strongly at small Ra_F^* but more weakly at larger Ra_F^* . As Eq. (28) shows, these trends must go hand-in-hand; consistency between the two quantities requires the trend in C to steepen if that in ϵ flattens. Moreover, for both C and ϵ , these changes in the slopes with Ra_F^* are precisely the ingredients that can generate a regime shift wherein Rossby numbers depend strongly on Ra_F^* at low Ra_F^* (as postulated for Regime II in Section 4b) but more weakly on Ra_F^* at high Ra_F^* (as postulated for Regime I in Section 4a). Third, the data suggest that, at constant Ra_F^* , the correlation coefficient increases with increasing E .

The theoretical curves for C and ϵ match the data surprisingly well (Fig. 6). All the qualitative trends discussed above for the data are predicted by the theory: C decreases and ϵ increases with Ra_F^* ; the slope of $C(Ra_F^*)$ steepens toward the right while that of $\epsilon(Ra_F^*)$ flattens toward the right; and at constant Ra_F^* the values of C increase with E . The theory also predicts that at constant Ra_F^* , the values of ϵ should decrease with increasing E ,

⁸ The correlation coefficient and jet-pumping efficiency were calculated from the anelastic simulations as

$$C = \frac{[\overline{u'v'_s}]}{([\overline{u'^2 v'^2}]^{1/2})}$$

and

$$\epsilon = \frac{[\overline{\bar{u} \frac{1}{\rho} \nabla \cdot (\bar{\rho} u' \mathbf{v}')}] }{[g w \alpha \delta T]}$$

where $[\dots] = \int (\dots) \bar{\rho} s ds / \int \bar{\rho} s ds$ indicates a mass-weighted average over the equatorial plane.

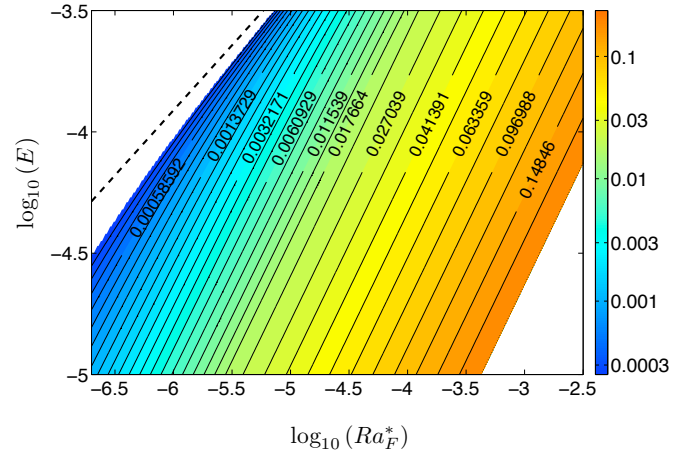


FIG. 7. Prediction of our scaling law, Eq. (33), that combines Regimes I and II. Depicts contours of Rossby number versus modified flux Rayleigh number (abscissa) and Ekman number (ordinate). Adopts $kD = 5\pi$, $\gamma = 1$, and $\epsilon_{\max} = 0.3$ (see text). Note the similarity of the slopes and values of the contours with the simulation results plotted in Fig. 3. Contours are evenly spaced in $\log(Ro)$, with contour values identical to those in Figs. 3 and 4. For reference, the dashed line depicts the critical modified flux Rayleigh number given by Eq. (24). Above the dashed line, convection does not occur.

which can be tested with future simulations. Moreover, for the parameters chosen ($\gamma = 1$ and $\epsilon_{\max} = 0.3$), the numerical values of the theoretical ϵ and C curves agree relatively well with the simulation data, particularly for the anelastic simulations at $E = 4 \times 10^{-4}$. On the other hand, the theoretical correlation coefficients at $E = 10^{-5}$ overpredict those for the corresponding Boussinesq simulations by up to a factor of several, particularly at the higher- Ra_F^* values. Of course, the technique adopted to smooth between the two regimes (cf Eqs. 31–32) will affect the degree to which the curves agree with the data, so the details of the comparisons should be considered tentative.

What are the implications of this discussion for the jet speeds? Inserting our expression for ϵ into Eq. (18) or our expression for C into Eq. (23) leads to a single, self-consistent expression for the Rossby number spanning both regimes. For simplicity, we adopt Eqs. (29)–(30) rather than their smoothed counterparts, leading to the expression

$$Ro = \frac{1}{kD} \min \left[\gamma^2 \frac{Ra_F^* - Ra_F^{*\text{crit}}}{E}, \epsilon_{\max}^{1/2} \left(\frac{Ra_F^* - Ra_F^{*\text{crit}}}{E} \right)^{1/2} \right]. \quad (33)$$

which is equivalent to the minimum of Eqs. (18) and (23). Thus, arguments based on energetics and momentum arguments are now self-consistent: both approaches pre-

dict that the Rossby number scales as $(Ra_F^* - Ra_F^{*\text{crit}})/E$ at weakly supercritical Rayleigh numbers but as $(Ra_F^* - Ra_F^{*\text{crit}}/E)^{1/2}$ at strongly supercritical Rayleigh numbers.

Figure 7 plots the jet speed predicted by Eq. (33) as contours of Rossby number versus Ra_F^* and E , with a contour spacing that is even in $\log(Ro)$ and contour values identical to those in Figs. 3 and 4. Regime I, in which the jet-pumping efficiency ϵ is constant, lies toward the lower right, while Regime II, in which the correlation coefficient C is constant, lies toward the upper left. The transition between the regimes manifests visually as a jump in the spacing of the constant- Ro contours and occurs at a Rossby number of ~ 0.02 for the parameters chosen, roughly consistent with the regime transition in the simulated data (see Fig. 3). Within Regime II, the slopes of the contours decrease as the Rossby number is decreased and the modified flux Rayleigh number approaches the critical value. A similar decrease in the slope of the contours at small Rossby number is evident in Christensen (2002)'s data plotted in Fig. 3. Moreover, throughout most of the parameter space accessed by the simulations, the predicted Rossby number (Fig. 7) matches those obtained in the simulations (Fig. 3) within a factor of ~ 2 .

5. Scaling for the jet speeds in Regime III: the asymptotic regime

The simulated behavior in Fig. 3 is reasonably well explained by the theory presented in Section 4, where Rossby numbers scale approximately with $(Ra_F^* - Ra_F^{*\text{crit}})/E$ at low Rayleigh numbers (Regime II) and as $(Ra_F^*/E)^{1/2}$ at high Rayleigh numbers (Regime I). However, Christensen (2002) argued that at the highest Ra_F^* he explored for each value of E (or equivalently the lowest E values explored for each value of Ra_F^*) his simulations approached an asymptotic regime where the mean equilibrated jet speed became independent of the values of the diffusivities and depend only weakly on the heat flux. This behavior manifests in Fig. 3(*top*) as both a widening of the constant- Ro contours and significant increase in their slope beyond one toward the far right edge of the plot, neither of which is predicted by the scalings in Section 4. Based on an empirical fit to his simulation results, Christensen (2002) proposed that in this asymptotic limit—which we call Regime III—the Rossby number associated with the characteristic jet speeds scales as⁹

$$Ro = 0.53(Ra_F^*)^{1/5}. \quad (34)$$

At present, however, a physical basis for this empirical fit is lacking. To see whether Eq. (34) can be theoretic-

ally explained, we present here a scaling analysis based on mixing-length theory. We compare it to available simulations and evaluate its implications for the Jovian parameter regime. Nevertheless, we emphasize at the outset that the existence of the asymptotic regime is tentative, and further numerical work is required to confirm (or refute) its existence and determine its properties. This section is intended simply to offer some ideas on how such an asymptotic regime, if it exists, could work.

We hypothesize that, if the viscosity is sufficiently small, the damping will be determined not by the molecular viscosity but by an eddy viscosity associated with turbulent diffusion. The concept of an eddy viscosity is relevant only when the convection is sufficiently supercritical (so that the eddies behave in a nonlinear, turbulent manner), leading us to adopt the approach of Section 4*a*. To obtain an expression for mean wind speed, we again equate forcing (Eq. 14) and damping (Eq. 15) but use the eddy viscosity, ν_{eddy} , in place of ν in Eq. (15). We adopt a standard mixing-length formulation for the eddy viscosity, $\nu_{\text{eddy}} \approx wk_{\text{mix}}^{-1}$, where w is the convective velocity (given by Eqs. 9–10) and k_{mix} is the wavenumber associated with the mixing length (e.g., a typical distance traversed by coherent convective plumes). In the case of a Boussinesq fluid, where α and ρ are constant and F , g , and c_p are approximately constant, this yields

$$u \sim \frac{\epsilon^{1/2}\Omega^{1/4}k_{\text{mix}}^{1/2}}{k\gamma^{1/2}} \left(\frac{\alpha g F}{\rho c_p} \right)^{1/4} \quad (35)$$

where ϵ is assumed approximately constant as in Section 4*a*. For an anelastic fluid, where α and ρ vary greatly with radius, we follow the approach used in Section 4*a*, yielding

$$u \sim \frac{\epsilon^{1/2}\Omega^{1/4}}{k\gamma^{1/2}} \left[\frac{\int \frac{\alpha g F}{c_p} r^2 dr}{\int \left(\frac{\alpha g F}{c_p} \right)^{1/2} k_{\text{mix}}^{-1} \rho^{1/2} r^2 dr} \right]^{1/2}. \quad (36)$$

Let us nondimensionalize these expressions so that they can be compared with existing Boussinesq and anelastic numerical results and the empirical asymptotic scaling (Eq. 34) proposed by Christensen (2002). Defining the Rossby number as $Ro \equiv u/(\Omega D)$ and assuming that k_{mix} is constant and that $Ra_F^* \gg Ra_F^{*\text{crit}}$, Eqs. (35)–(36) can be nondimensionalized to yield

$$Ro = \frac{\epsilon^{1/2}\Gamma(k_{\text{mix}}D)^{1/2}}{kD\gamma^{1/2}} (Ra_F^*)^{1/4} \quad (37)$$

where Ra_F^* is given by Eq. (5) for the Boussinesq case and Eq. (7) for the anelastic case. Γ is a dimensionless constant that depends on the planet's basic-state radial

⁹Because he included an inner-to-outer radius ratio in his definition of Ra_F^* , Christensen (2002) quotes the relationship with a pre-factor of 0.65 rather than 0.53.

density structure and is given by

$$\Gamma = \left[\frac{(\int \rho r^2 dr)^{1/2} \left(\int \frac{\alpha g f}{c_p} r^2 dr \right)^{1/2}}{\int \left(\frac{\alpha g f}{c_p} \right)^{1/2} \rho^{1/2} r^2 dr} \right]^{1/2} \quad (38)$$

where $f(r)$ is an order-unity dimensionless function that describes the radial dependence of the heat flux, $F = F_0 f(r)$, and F_0 is a constant (independent of radius) that gives the characteristic value of the heat flux (e.g., halfway through the layer). Note that, for the case of constant ρ , α , g , flux, and c_p , then $\Gamma \equiv 1$. Interestingly, for the Kaspi et al. (2009) model, $\Gamma = 1.02$ despite the large variation of α and ρ with radius.¹⁰

This simple theory therefore predicts that, in the asymptotic regime, the characteristic jet speed scales as $F^{1/4}$, or equivalently the characteristic Rossby number scales as $(Ra_F^*)^{1/4}$, with no explicit dependence on the molecular or numerical viscosity. Our exponent of 1/4 compares favorably to—but is modestly steeper than—Christensen’s empirically determined exponent of 1/5. Notably, our theoretical exponent is significantly smaller than that for Regimes I and II (Section 4), where, at constant E , jet speeds scale with $F^{1/2}$ or F depending on assumptions. In our asymptotic theory, the weak dependence on Ra_F^* occurs because the eddy viscosity decreases with decreasing heat flux (unlike the behavior in Regimes I and II, where the viscosity is a fixed parameter). As a result, a weakly forced flow has extremely weak damping, whereas a strongly forced flow has extremely strong damping; this leads to an equilibrated jet speed that depends only weakly on heat flux. Specifically, the kinetic-energy forcing scales with F , and because the convective velocities scale with $F^{1/2}$ (Eq. 9), the eddy viscosity and therefore the kinetic-energy damping also scale with $F^{1/2}$. This leads to an equilibrated kinetic energy scaling with $F^{1/2}$ and a jet speed scaling with $F^{1/4}$.

Figure 8 explicitly compares the theoretical scaling (Eq. 37) with the empirical scaling (Eq. 34) and the simulation results of Christensen (2002) and Kaspi et al. (2009). The theoretical scaling is shown for a value of the prefactor $\epsilon^{1/2}(k_{\text{mix}}D)^{1/2}\gamma^{-1/2}(kD)^{-1}$, which we call χ , equal to 1. For this value, the magnitudes of the jet speeds predicted by our Eq. (37) match Christensen’s fit within a factor of ~ 2 (compare solid and dashed lines in Fig. 8a). For the values of $kD \approx 5\pi$ adopted previously, this would require $k_{\text{mix}} \approx (5\pi)^2/D$, implying a rather short mixing length $2\pi k_{\text{mix}}^{-1}$ of $\sim 0.03D$. This seems at

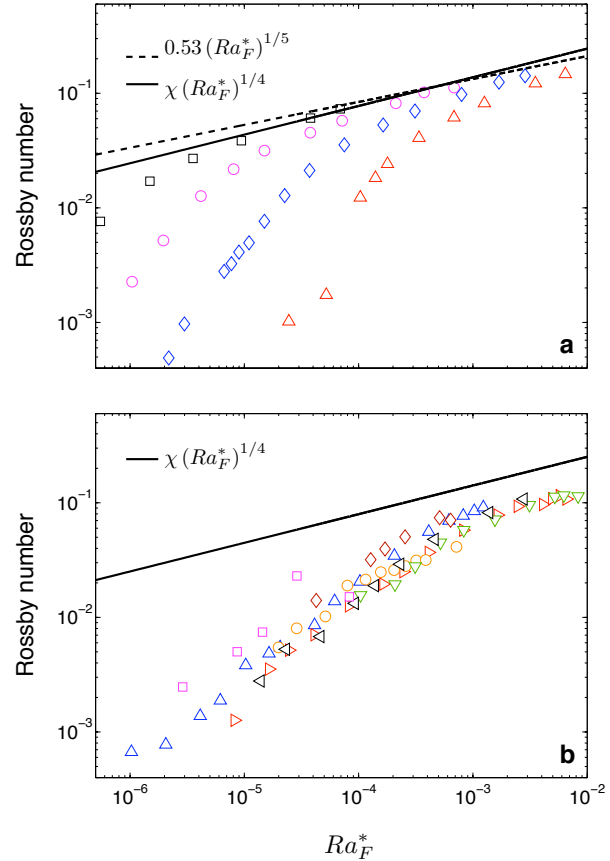


FIG. 8. Comparison of our asymptotic scaling for the jet speeds, Eq. (37) (solid curves) with Christensen’s empirical asymptotic fit from Eq. (34) (dashed curve) and simulation results from Christensen (2002) (panel a) and Kaspi et al. (2009) (panel b). Solid curves are evaluated using $\epsilon = 0.3$, $\gamma = 1$, and $\chi = 1$. See Table 1 for definitions of the symbols used in (b).

¹⁰Given the integrals in the numerator and denominator of Γ , one can show that Γ tends to be close to 1 for a wide range of possible radial dependences of the function $\alpha g f/c_p$ —even when this function varies in radius by orders of magnitude—as long as it has a smooth dependence, as occurs in the numerical models and in Jupiter.

least qualitatively consistent with the fact that the vorticity structure of convective plumes exhibits little coherence in cylindrical radius s (see Christensen 2002). The eddy diffusivities implied by this choice of mixing length are similar to those suggested by previous authors, lending some encouragement to this choice of prefactor.¹¹

Overall, the close agreement between the heat-flux dependences of our asymptotic scaling and Christensen’s empirical fit is encouraging and argues that the basic idea encapsulated by our scaling—that the damping depends on F to a power modestly less than that of the forcing—is correct.

At high Rayleigh numbers, both the Boussinesq and anelastic simulations (Fig. 8a and b, respectively) converge toward a trend similar to the shallow slope of the predicted asymptotic scaling. However, the simulations diverge from the asymptotic scalings at low Rayleigh numbers as the effects of the model diffusivities become strong. Christensen’s fit, and the scaling presented in this section, are intended to describe the *asymptotic* behavior in the limit of negligible diffusivities (for discussion see Christensen 2002).

When extrapolated to Jovian values of Ra_F^* , this asymptotic regime predicts that the mass-weighted mean velocities in the molecular envelopes of Jupiter and Saturn are small, $\sim 0.1\text{--}1\text{ m sec}^{-1}$. We consider this issue further, and combine the three regimes into a single scaling, in the next subsection.

6. Combining the three scalings

We have derived scalings for the jet speeds in three regimes: two regimes in which the numerical viscosity dominates the damping (Regimes I and II in Sections 4a and 4b, respectively) and another in which the viscosity is determined by turbulence, i.e., an eddy viscosity (Regime III in Section 5). Here, we combine the scalings.

Our basic approach in deriving the scalings was to balance forcing against damping; the damping represents a numerical (or molecular) viscosity in Regime I but an eddy viscosity in Regime III. Here, we suppose that both molecular and eddy viscosities operate simultaneously, and that whichever viscosity is larger will dominate. Because larger viscosity implies smaller equilibrated jet speeds, we therefore expect that the *smaller*

of the two Rossby numbers will dominate. Combining Regimes I, II, and III, we can thus roughly say

$$Ro = \frac{1}{kD} \min \left[\gamma^2 \frac{Ra_F^* - Ra_F^{*\text{crit}}}{E}, \epsilon_{\text{max}}^{1/2} \left(\frac{Ra_F^* - Ra_F^{*\text{crit}}}{E} \right)^{1/2}, \epsilon_{\text{max}}^{1/2} \Gamma \frac{(k_{\text{mix}}D)^{1/2}}{\gamma^{1/2}} (Ra_F^*)^{1/4} \right] \quad (39)$$

where we have assumed that k is constant and ϵ_{max} has the same values in the second and third terms on the right side. Neglecting $Ra_F^{*\text{crit}}$ in the expression for Regime I, the transition between Regimes I and III occurs for Ekman numbers

$$E_{\text{tr}} \approx \frac{\gamma (Ra_F^*)^{1/2}}{\Gamma^2 k_{\text{mix}} D}. \quad (40)$$

At a given Ra_F^* , Regime I (or II) occurs for large Ekman numbers while the asymptotic regime occurs for small Ekman numbers, with a transition near E_{tr} . Analogously, at constant E , Regime I (or II) dominates at small Ra_F^* while the asymptotic regime occurs at large Ra_F^* , with a transition near modified flux Rayleigh numbers of $\Gamma^4 \gamma^{-2} (k_{\text{mix}} D)^2 E^2$.

To illustrate the combined scaling, Fig. 9 depicts Eq. (39) as contours of Rossby number versus Ra_F^* and E for the specific case $\epsilon_{\text{max}} = 0.3$, $\gamma = 1$, and $kD = 5\pi$ (the same values as in all previous figures). The value of k_{mix} is chosen so that the prefactor in the asymptotic regime $\epsilon_{\text{max}}^{1/2} (k_{\text{mix}} D)^{1/2} (\gamma^{1/2} kD)^{-1} \equiv \chi = 1$. Regimes II and I lie in the upper left and exhibit sloped contours. The asymptotic regime lies at the lower right and exhibits vertical contours, consistent with the expectation that Rossby number is independent of E there. As expected from Eq. (40), the transition between Regimes I and III slopes gradually upward to the right; the asymptotic regime extends to larger E when Ra_F^* is larger. For the value of k_{mix} adopted in Fig. 9, Christensen’s simulations lie predominantly within Regimes I and II; however, the predicted transition to the asymptotic regime occurs close to Christensen’s highest- Ra_F^* cases for each value of E . If Fig. 9 is correct, it would suggest that the asymptotic regime would become clear at Ekman numbers an order of magnitude smaller than Christensen explored for each value of Ra_F^* . Note, however, that in reality the transition between the regimes will probably occur smoothly across a broad strip straddling $E_{\text{tr}}(Ra_F^*)$; if so, it might be necessary to reach Ekman numbers as low as 10^{-7} to see the asymptotic regime clearly.

Now we examine Fig. 10a, which plots our combined scaling (Eq. 39) versus Ra_F^* for several values of E and compares them to Christensen (2002)’s Boussinesq simulations. Curves and simulation data are shown for $E = 10^{-5}$ (black), 3×10^{-5} (magenta), 10^{-4} (blue),

¹¹The (dimensional) eddy diffusivity implied by our expression for vertical velocity (Eq. 9) and the condition $\chi = 1$ is $\nu_{\text{eddy}} \approx \epsilon D (\alpha g F)^{1/2} / [(\rho c_p \Omega)^{1/2} \gamma (kD)^2]$. For Jovian interior conditions and heat flux ($\alpha \approx 10^{-5} \text{ K}^{-1}$, $g \approx 26 \text{ m sec}^{-2}$, $F = 5 \text{ W m}^{-2}$, $\rho \approx 1000 \text{ kg m}^{-3}$, $c_p \approx 1.3 \times 10^4 \text{ J kg}^{-1} \text{ K}^{-1}$, $\Omega = 1.74 \times 10^{-4} \text{ sec}^{-1}$, $D = 2 \times 10^4 \text{ km}$), and $\epsilon = 0.3$ and $kD = 5\pi$ as adopted previously, this implies values of $\sim 20 \text{ m}^2 \text{ sec}^{-1}$. This is roughly consistent with the value of $\sim 10 \text{ m}^2 \text{ sec}^{-1}$ suggested by Starchenko and Jones (2002).

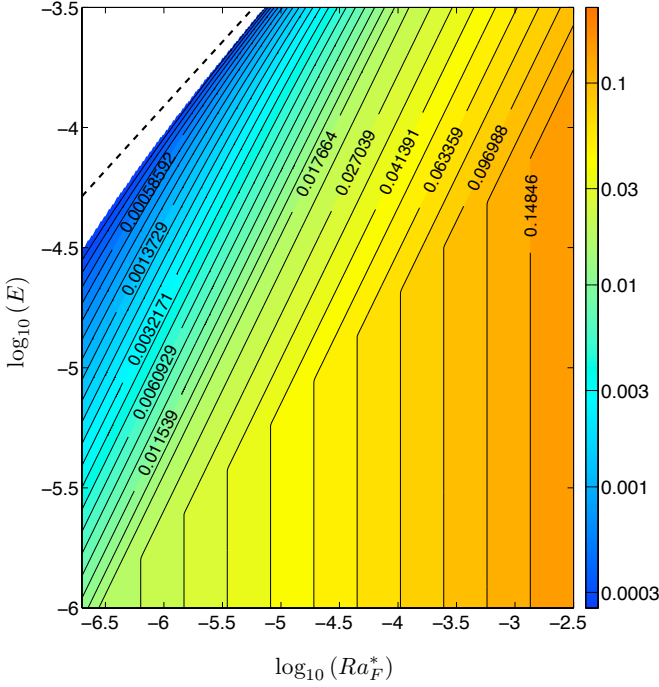


FIG. 9. Predicted jet speeds for a scaling law that combines Regimes I, II, and III, given in Eq. (39), for the case $\epsilon_{\max} = 0.3$, $kD = 5\pi$, and $\gamma = 1$. The value of k_{mix} is chosen so that the prefactor in the asymptotic regime, $\chi \equiv \epsilon_{\max}^{1/2} (k_{\text{mix}} D)^{1/2} / (\gamma^{1/2} kD)$, equals one. Depicts contours of Rossby number versus modified flux Rayleigh number (abscissa) and Ekman number (ordinate). In the Regimes I and II, contours tilt upward to the right, whereas in the asymptotic regime they are vertical. For reference, the dashed line depicts the critical modified flux Rayleigh number given by Eq. (24). Above the dashed line, convection does not occur.

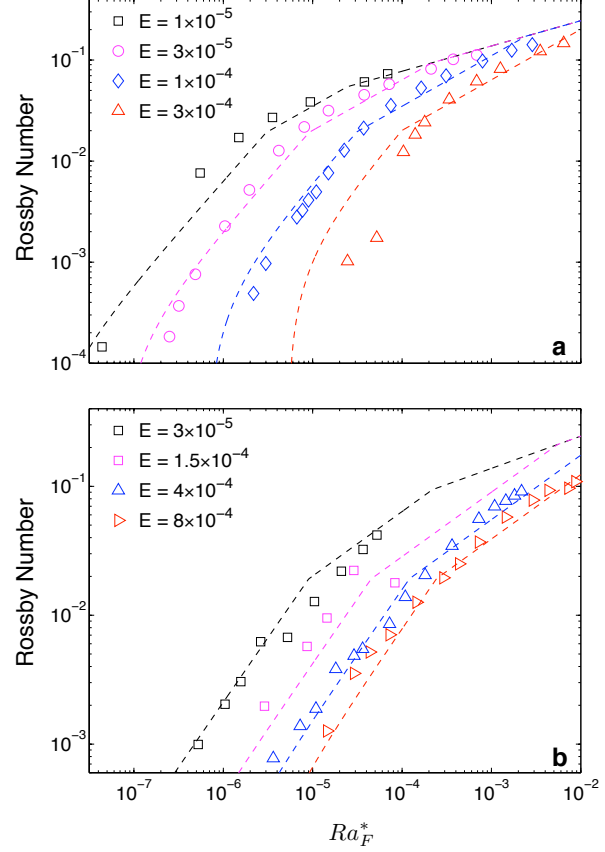


FIG. 10. Predicted jet speeds for a scaling law that combines Regimes I, II, and III, given in Eq. (39), for the case $\epsilon_{\max} = 0.3$, $kD = 5\pi$, and $\chi = 1$. Depicts Rossby number versus modified flux Rayleigh number for several values of E for our combined scaling (curves) and from simulations (symbols). Panel *a*: Christensen (2002)'s Boussinesq simulations, at Ekman numbers of 1×10^{-5} , 3×10^{-5} , 10^{-4} , and 3×10^{-4} , with scaling predictions evaluated at those same values (plotted in the corresponding colors). Panel *b*: Anelastic simulations at Ekman numbers of 1.5×10^{-4} , 4×10^{-4} , and 8×10^{-4} , along with a Boussinesq simulation at 3×10^{-5} , performed using the Kaspi et al. (2009) model. Curves give scaling predictions evaluated at those same values (plotted in corresponding colors). The combined scaling matches (to within a factor of ~ 2) the mass-weighted mean jet speeds obtained in both the Boussinesq and anelastic simulations over a factor of 10^5 in Ra_F^* , 10^2 in Ekman number, and 10^3 in Rossby number.

and 3×10^{-4} (red). The three regimes are clearly visible in the scalings and agree favorably with the simulations throughout the plotted range. The gradual increase in the slopes in Regime II near the left edge—which can be seen in both the scalings and the simulations, especially at Ekman numbers of 3×10^{-5} and 10^{-4} —results from the fact that Ra_F^* approaches its critical value (evaluated for the scalings using Eq. 24). Although the match is not perfect, the scalings not only approximately reproduce the asymptotic behavior suggested by Christensen but also exhibit the trend (suggested by Christensen’s simulations) where the transition to the asymptotic regime occurs at larger Ra_F^* for larger E . The values of Ra_F^* at these transitions are similar in the scalings as in Christensen’s simulations to within an order of magnitude for most E values. Moreover, the actual values of Rossby number predicted by the scaling at a given Ra_F^* and E match those of Christensen’s simulations to within a factor of ~ 2 .

Figure 10*b* compares our combined scaling against simulations performed using the Kaspi et al. (2009) model. Magenta squares, blue upward-pointing triangles, and red right-pointing triangles present the Rossby numbers from anelastic simulations performed respectively at $E = 1.5 \times 10^{-4}$, 4×10^{-4} , and 8×10^{-4} using the Jovian radial structure as in Kaspi et al. (2009), while the black squares present Rossby numbers from a Boussinesq simulation at $E = 3 \times 10^{-5}$ performed with the same model. Scaling predictions are overplotted in the corresponding colors (black, magenta, blue, and red for Ekman numbers of 3×10^{-5} , 1.5×10^{-4} , 4×10^{-4} , and 8×10^{-4} , respectively). In these runs, the Prandtl number equals 10, leading to a smaller critical Rayleigh number than given in Eq. (24); as a result, the plotted ranges are sufficiently supercritical that the scaling predictions do not exhibit a gradual change in slope near the left edge of the plot (in contrast to the behavior in panel *a*). Again, the scalings agree well with the simulations; the discrepancy is everywhere less than a factor of 2. This agreement is encouraging considering that, together, Fig. 10*a* and *b* present results spanning factors of 200,000 in Ra_F^* , 1000 in Ro , and 80 in E .

Importantly, when the modified flux Rayleigh number is defined in the appropriate mass-weighted way (Eq. 7), the *same scalings* explain the mass-weighted, global-mean Rossby numbers of *both* the Boussinesq and anelastic simulations, despite the fact that the former use constant mean density while the latter adopt background densities (and thermal expansivities) that vary radially by several orders of magnitude from top to bottom. The Boussinesq simulations exhibit relatively little axial shear of the zonal wind along columns of constant s (Christensen 2002), while the anelastic simulations described here exhibit significant shear (Kaspi et al. 2009). The fact that

our scaling arguments can explain both sets of runs indicates that this shear (if present) does not control the mass-weighted mean interior wind speed.

Interestingly, Fig. 9 suggests that Regime I disappears for sufficiently small Ekman and modified flux Rayleigh numbers ($E \leq 10^{-7}$ and $Ra_F^* \leq 10^{-8}$ for the parameters chosen). If so, then at very small Ekman numbers, Regime II abuts directly against Regime III. No numerical simulations have yet been performed at these small parameter values, however, and how this transition occurs remains an open question. Equation (39) may need modification in this low- Ra_F^* and low- E portion of the parameter space pending further numerical and theoretical work.

Next, we extrapolate the scalings to Jupiter, where the Ekman and modified flux Rayleigh numbers are $\sim 10^{-15}$ and $\sim 10^{-13}$ – 10^{-14} , respectively. Despite the uncertainties, Eq. (39) would suggest that Jupiter lies in the asymptotic regime. For the Jovian values of Ra_F^* and E , the scalings predict Rossby numbers of $\sim 3 \times 10^{-5}$ – 6×10^{-4} and the implied zonal wind speeds in the interior are ~ 0.1 – 1 m sec $^{-1}$. Although numerical simulations that are overforced by orders of magnitude can easily produce Jupiter-like jet speeds (Christensen 2001, 2002; Heimpel and Aurnou 2007), both Christensen’s asymptotic fit and our mixing-length scalings therefore suggest that, given the weakly forced conditions of Jupiter’s interior, the zonal-jet speeds in the interior are much slower than the observed cloud-level values (which reach ~ 150 m sec $^{-1}$ for Jupiter and 400 m sec $^{-1}$ for Neptune). Nevertheless, this conclusion is tentative, because our estimates of eddy viscosity are uncertain and because the asymptotic regime (if it exists!) is not yet obvious in numerical simulations. Stronger confirmation of the existence or absence of the asymptotic regime in numerical models is necessary.

7. Conclusions

Over the past two decades, several authors have performed three-dimensional numerical simulations of low-viscosity convection in rapidly rotating spherical shells to test the hypothesis that convection in the molecular interiors pumps the fast zonal jet streams observed on Jupiter, Saturn, Uranus, and Neptune. These studies show that the zonal jet speeds can range over many orders of magnitude depending on the heat flux, viscosity, and other parameters (e.g., Christensen 2002; Kaspi et al. 2009). Here, we presented simple theoretical arguments to explain the characteristic jet speeds—and their dependence on heat flux and viscosity—seen in these studies.

Our main findings are as follows:

- We demonstrated that the characteristic convective velocities in the Kaspi et al. (2009) simulations

scale well with $(\alpha g F / \rho c_p \Omega)^{1/2}$. While such a rotating scaling has long been proposed and is consistent with rotating laboratory experiments (e.g., Fernando et al. 1991), this to our knowledge is the first demonstration of its applicability to the interiors of giant planets over a wide range of heat fluxes and rotation rates.

- Next, we attempted to explain the jet speeds obtained by Christensen (2002) and Kaspi et al. (2009) in three-dimensional numerical simulations of convection with free-slip boundaries. At weakly supercritical Rayleigh numbers, linear theory (e.g., Busse 1983a; Busse and Hood 1982) and numerical simulations (e.g., Christensen 2002) show that the eastward and outward convective velocity components are highly correlated outside the tangent cylinder. We showed that if the degree of correlation C between the eastward and outward convective velocity components is constant (as expected at very low supercriticalities) and if the jets are damped by a numerical viscosity, then the mean jet speeds should scale as the convective heat flux over the viscosity (Regime II). This scaling explains the jet speeds obtained in both Boussinesq and anelastic simulations at low Rayleigh numbers, where the jet speeds are relatively weak.
- On the other hand, at higher Rayleigh number, the eastward and outward convective velocity components become increasingly decorrelated. We showed that, if the fraction of convective energy release used to pump the jets (ϵ) is a constant in this regime, and if the jets are damped by a numerical viscosity, then the mean jet speeds should scale as $(F/\nu)^{1/2}$. This scaling (Regime I) explains quite well the mean jet speeds obtained in the simulations from Christensen (2002) and Kaspi et al. (2009) in cases when the jets dominate the total kinetic energy, as occurs at highly supercritical Rayleigh numbers.
- The relationship between the correlation coefficient C and the jet-pumping efficiency ϵ shows how the transition between these two regimes can naturally occur. A nearly constant correlation coefficient implies that the jet-pumping efficiency must increase strongly with Ra_F^* . When the jet-pumping efficiency finally plateaus near its maximum value of 1, then the correlation coefficient must begin to decrease strongly with further increases in Ra_F^* (see Eq. 28). Thus, a natural regime transition occurs between Regime II at low Rayleigh numbers and Regime I at high Rayleigh numbers. Moreover, we rigorously calculated C and ϵ from the anelastic

simulations and showed that, as expected, C decreases and ϵ increases with Ra_F^* . A simple, heuristic theory that transitions smoothly between constant correlation coefficient at low Ra_F^* and a constant jet-pumping efficiency at high Ra_F^* explains the qualitative features of the correlation coefficient and jet-pumping efficiency as calculated from the simulations.

- Both the Boussinesq (Christensen 2002) and anelastic simulations hint at the existence of a third regime where, at sufficiently large heat flux and/or sufficiently small viscosity, the characteristic jet speeds become independent of the viscosity. We constructed a simple mixing-length scaling for the behavior in this regime under the assumption that the jet-pumping efficiency is constant and the damping results from an eddy viscosity (rather than the molecular or numerical viscosity). This scaling suggests that the mean jet speed in the molecular interior should scale with the convective heat flux to the 1/4 power. Given the simplicity of our model, this agrees favorably with the asymptotic fit suggested by Christensen (2002), which proposes that jet speeds should scale with the convective heat flux to the 1/5 power. Both scalings suggest—tentatively—that the mean wind speeds in the molecular interior should be significantly weaker than the jet speeds measured at the cloud level.
- A scaling that combines these three regimes can explain (to within a factor of ~ 2) the mass-weighted mean jet speeds obtained in both the Boussinesq and anelastic simulations ranging across a factor of 10^5 in Ra_F^* , 10^2 in Ekman number, and 10^3 in Rossby number. Importantly, when the modified flux Rayleigh number is defined in an appropriate mass-weighted way, the *same scalings* apply to both Boussinesq and anelastic cases.

It is important to emphasize that the scaling theories presented in Sections 4–6 apply only to the mass-weighted mean wind speeds. The theory does not provide information on the detailed three-dimensional structure of the jets, such as their variation in latitude.

Several challenges remain for the future. First, we did not consider the effect of the Prandtl number on the jet speeds, mostly because a careful characterization of the Ra_F^* - and E -dependence of the jet speeds over a wide range has only been performed for a very limited number of Pr values (1 for Christensen (2002) and 10 for Kaspi et al. (2009)). However, several studies show that Pr does affect the jet speeds (e.g., Aubert et al. 2001; Christensen 2002; Kaspi 2008), although one would expect this

dependence to disappear in the asymptotic limit. Extending our scalings to include the Pr dependence is an important goal for future work.

Second, the simulations we set out to explain—those of Christensen (2002) and Kaspi et al. (2009)—assume the convection occurs in a thick shell, for which the region outside the tangent cylinder dominates the total mass, volume, and kinetic energy. As shown by several authors, however, the dynamical mechanisms and details of jet pumping differ for the fluid inside and outside the tangent cylinder (e.g., Heimpel and Aurnou 2007). Thus, the scaling properties could differ for simulations in a thin shell (Heimpel and Aurnou 2007; Heimpel et al. 2005), for which the high-latitude regions inside the tangent cylinder will more strongly influence mass-weighted mean flow properties.

Third, we assumed that the wavenumber k —which represents the length scale for the variation of zonal-wind shear and Reynolds stress with cylindrical radius s —was a constant with the Rayleigh and Ekman numbers. To zeroth order, this seems a reasonable approximation, because simulations suggest that the widths of the jets outside the tangent cylinder are set by the adopted shell thickness and not by the Ekman and Rayleigh numbers.¹² Nevertheless, analytic solutions in the linear limit suggest that the zonal wavelengths near the critical Rayleigh number should scale as $E^{1/3}$ (e.g., Busse 1970; Roberts 1968), and scaling arguments in the context of convection with no-slip boundaries suggest that the sizes of vortex rolls scale as $E^{1/5}$ (Aubert et al. 2001). Thus, the wavenumber representing the s -variation of the zonal-jet-shear and Reynolds stresses could potentially have a weak dependence on E . Although our assumption of constant k seems to work reasonably well over the simulated range, it would be worth relaxing this assumption in the future.

Our scaling arguments—and the simulations they attempt to explain—assume the fluid is electrically neutral. However, the interiors of Jupiter and Saturn become metallic at pressures exceeding ~ 1 Mbar (Guillot et al. 2004), and the resulting magnetohydrodynamic effects could influence the jet dynamics even in the molecular region (e.g., Glatzmaier 2008; Kirk and Stevenson 1987; Liu et al. 2008). For example, Liu et al. (2008) argued that Ohmic dissipation would limit strong jets to regions above 96% (86%) of the radius on Jupiter (Saturn). They further argued that, if the interior is isentropic and exhibits columnar Taylor-Proudman behavior, the winds would be weak not only in the electrically conducting region but throughout the convection zone. This result is consistent with ours although it invokes different physics.

Moreover, the simulations we investigated do not include solar forcing or latent heating. These effects may induce significant internal density perturbations—and therefore thermal-wind shear—within a few scale heights of the observable cloud deck (e.g., Kaspi and Flierl 2007; Lian and Showman 2008, 2010; Schneider and Liu 2009; Williams 2003). The development of convective models that include these effects is a major goal for the future.

Acknowledgments. This work was supported by NSF grant AST-0708698 and NASA grants NNX07AF35G and NNX10AB91G to APS, NSF grant AST-0708106 to GRF, and a NOAA Climate and Global Change Postdoctoral Fellowship to YK administered by the University Corporation for Atmospheric Research.

REFERENCES

- Atkinson, D. H., A. P. Ingersoll, and A. Seiff, 1997: Deep zonal winds on Jupiter: Update of Doppler tracking the Galileo probe from the orbiter. *Nature*, **388**, 649–650.
- Aubert, J., 2005: Steady zonal flows in spherical shell dynamos. *Journal of Fluid Mechanics*, **542**, 53–67.
- Aubert, J., D. Brito, H. Nataf, P. Cardin, and J. Masson, 2001: A systematic experimental study of rapidly rotating spherical convection in water and liquid gallium. *Physics of the Earth and Planetary Interiors*, **128**, 51–74.
- Aurnou, J., S. Andreadis, L. Zhu, and P. Olson, 2003: Experiments on convection in Earth’s core tangent cylinder. *Earth and Planetary Science Letters*, **212**, 119–134.
- Aurnou, J., M. Heimpel, and J. Wicht, 2007: The effects of vigorous mixing in a convective model of zonal flow on the ice giants. *Icarus*, **190**, 110–126.
- Aurnou, J., M. Heimpel, L. Allen, E. King, and J. Wicht, 2008: Convective heat transfer and the pattern of thermal emission on the gas giants. *Geophysical Journal International*, **173**, 793–801.
- Aurnou, J. M., and M. H. Heimpel, 2004: Zonal jets in rotating convection with mixed mechanical boundary conditions. *Icarus*, **169**, 492–498.
- Aurnou, J. M., and P. L. Olson, 2001: Strong zonal winds from thermal convection in a rotating spherical shell. *Geophys. Res. Lett.*, **28**, 2557–2560.
- Boubnov, B. M., and G. S. Golitsyn, 1990: Temperature and velocity field regimes of convective motions in a rotating plane fluid layer. *Journal of Fluid Mechanics*, **219**, 215–239.
- Busse, F. H., 1970: Thermal instabilities in rapidly rotating systems. *Journal of Fluid Mechanics*, **44**, 441–460.
- Busse, F. H., 1983a: Convection-driven zonal flows in the major planets. *Pure and Applied Geophysics*, **121**, 375–390.
- Busse, F. H., 1983b: A model of mean zonal flows in the major planets. *Geophysical and Astrophysical Fluid Dynamics*, **23**, 153–174.

¹²In the equatorial plane, the simulations generally exhibit westward flow at the inner boundary and eastward flow at the outer boundary, with a relatively smooth transition in between.

- Busse, F. H., 2002: Convective flows in rapidly rotating spheres and their dynamo action. *Physics of Fluids*, **14**, 1301–1314.
- Busse, F. H., and L. L. Hood, 1982: Differential rotation driven by convection in a rapidly rotating annulus. *Geophysical and Astrophysical Fluid Dynamics*, **21**, 59–74.
- Cardin, P., and P. Olson, 1994: Chaotic thermal convection in a rapidly rotating spherical shell: consequences for flow in the outer core. *Physics of the Earth and Planetary Interiors*, **82**, 235–259.
- Christensen, U. R., 2001: Zonal flow driven by deep convection in the major planets. *Geophys. Res. Lett.*, **28**, 2553–2556.
- Christensen, U. R., 2002: Zonal flow driven by strongly supercritical convection in rotating spherical shells. *Journal of Fluid Mechanics*, **470**, 115–133.
- Christensen, U. R., and J. Aubert, 2006: Scaling properties of convection-driven dynamos in rotating spherical shells and application to planetary magnetic fields. *Geophysical Journal International*, **166**, 97–114.
- Dornmy, E., A. M. Soward, C. A. Jones, D. Jault, and P. Cardin, 2004: The onset of thermal convection in rotating spherical shells. *Journal of Fluid Mechanics*, **501**, 43–70.
- Dowling, T. E., 1995: Estimate of Jupiter’s deep zonal-wind profile from Shoemaker-Levy 9 data and Arnold’s second stability criterion. *Icarus*, **117**, 439–442.
- Evonuk, M., 2008: The Role of Density Stratification in Generating Zonal Flow Structures in a Rotating Fluid. *Astrophys. J.*, , **673**, 1154–1159.
- Evonuk, M., and G. A. Glatzmaier, 2006: A 2D study of the effects of the size of a solid core on the equatorial flow in giant planets. *Icarus*, **181**, 458–464.
- Evonuk, M., and G. A. Glatzmaier, 2007: The effects of rotation rate on deep convection in giant planets with small solid cores. *Planet. Space Sci.*, **55**, 407–412.
- Fernando, H. J. S., R.-R. Chen, and D. L. Boyer, 1991: Effects of rotation on convective turbulence. *Journal of Fluid Mechanics*, **228**, 513–547.
- Glatzmaier, G. A., 2008: A note on “Constraints on deep-seated zonal winds inside Jupiter and Saturn”. *Icarus*, **196**, 665–666.
- Glatzmaier, G. A., M. Evonuk, and T. M. Rogers, 2009: Differential rotation in giant planets maintained by density-stratified turbulent convection. *Geophys. Astrophys. Fluid Dyn.*, **103**, 31–51.
- Golitsyn, G. S., 1980: Geostrophic Convection. *Doklady Akademii Nauk SSSR*, **251**, 1356–1360.
- Golitsyn, G. S., 1981: Convection structure during fast rotation. *Doklady Akademii Nauk SSSR*, **261**, 317–320.
- Guillot, T., D. J. Stevenson, W. B. Hubbard, and D. Saumon, 2004: The interior of Jupiter. *Jupiter: The Planet, Satellites and Magnetosphere*, F. Bagenal, T. E. Dowling, and W. B. McKinnon, Eds., Cambridge Univ. Press, pp. 35–57.
- Heimpel, M., and J. Aurnou, 2007: Turbulent convection in rapidly rotating spherical shells: A model for equatorial and high latitude jets on Jupiter and Saturn. *Icarus*, **187**, 540–557.
- Heimpel, M., J. Aurnou, and J. Wicht, 2005: Simulation of equatorial and high-latitude jets on Jupiter in a deep convection model. *Nature*, **438**, 193–196.
- Hubbard, W. B., W. J. Nellis, A. C. Mitchell, N. C. Holmes, P. C. McCandless, and S. S. Limaye, 1991: Interior structure of Neptune - Comparison with Uranus. *Science*, **253**, 648–651.
- Ingersoll, A. P., and D. Pollard, 1982: Motion in the interiors and atmospheres of Jupiter and Saturn - Scale analysis, anelastic equations, barotropic stability criterion. *Icarus*, **52**, 62–80.
- Jones, C. A., and K. M. Kuzanyan, 2009: Compressible convection in the deep atmospheres of giant planets. *Icarus*, **204**, 227–238.
- Kaspi, Y., 2008: Turbulent convection in an anelastic rotating sphere: A model for the circulation on the giant planets, Ph.D. thesis, Massachusetts Institute of Technology.
- Kaspi, Y., and G. R. Flierl, 2007: Formation of Jets by Baroclinic Instability on Gas Planet Atmospheres. *Journal of Atmospheric Sciences*, **64**, 3177–3194.
- Kaspi, Y., G. R. Flierl, and A. P. Showman, 2009: The deep wind structure of the giant planets: results from an anelastic general circulation model. *Icarus*, **202**, 525–542.
- Kaspi, Y., W. B. Hubbard, A. P. Showman, and G. R. Flierl, 2010: Gravitational signature of Jupiter’s internal dynamics. *Geophys. Res. Lett.*, , **37**, 1204–+.
- Kirk, R. L., and D. J. Stevenson, 1987: Hydromagnetic constraints on deep zonal flow in the giant planets. *Astrophys. J.*, , **316**, 836–846.
- Legarreta, J., and A. Sánchez-Lavega, 2008: Vertical structure of Jupiter’s troposphere from nonlinear simulations of long-lived vortices. *Icarus*, **196**, 184–201.
- Lian, Y., and A. P. Showman, 2008: Deep jets on gas-giant planets. *Icarus*, **194**, 597–615.
- Lian, Y., and A. P. Showman, 2010: Generation of equatorial jets by large-scale latent heating on the giant planets. *Icarus*, **207**, 373–393.
- Liu, J., P. M. Goldreich, and D. J. Stevenson, 2008: Constraints on deep-seated zonal winds inside Jupiter and Saturn. *Icarus*, **196**, 653–664.
- Morales-Juberias, R., and T. E. Dowling, 2005: Simulations of high-latitude spots on Jupiter: Constraints on vortex strength and the deep wind. *Planet. Space Sci.*, **53**, 1221–1233.
- Roberts, P. H., 1968: On the Thermal Instability of a Rotating-Fluid Sphere Containing Heat Sources. *Royal Society of London Philosophical Transactions Series A*, **263**, 93–117.
- Sánchez-Lavega, A., et al., 2008: Depth of a strong jovian jet from a planetary-scale disturbance driven by storms. *Nature*, **451**, 437–440.
- Saumon, D., G. Chabrier, and H. M. van Horn, 1995: An Equation of State for Low-Mass Stars and Giant Planets. *Astrophys. J. (Supp.)*, , **99**, 713–741.
- Schneider, T., and J. Liu, 2009: Formation of Jets and Equatorial Superrotation on Jupiter. *J. Atmos. Sci.*, **66**, 579–601.

- Starchenko, S. V., and C. A. Jones, 2002: Typical Velocities and Magnetic Field Strengths in Planetary Interiors. *Icarus*, **157**, 426–435.
- Stevenson, D. J., 1979: Turbulent thermal convection in the presence of rotation and a magnetic field - A heuristic theory. *Geophysical and Astrophysical Fluid Dynamics*, **12**, 139–169.
- Stevenson, D. J., 2003: Planetary magnetic fields. *Earth and Planetary Science Letters*, **208**, 1–11.
- Sun, Z., G. Schubert, and G. A. Glatzmaier, 1993: Transitions to chaotic thermal convection in a rapidly rotating spherical fluid shell. *Geophysical and Astrophysical Fluid Dynamics*, **69**, 95–131.
- Tilgner, A., and F. H. Busse, 1997: Finite-amplitude convection in rotating spherical fluid shells. *Journal of Fluid Mechanics*, **332**, 359–376.
- Vasavada, A. R., and A. P. Showman, 2005: Jovian atmospheric dynamics: an update after Galileo and Cassini. *Reports of Progress in Physics*, **68**, 1935–1996.
- Williams, G. P., 2003: Jovian Dynamics. Part III: Multiple, Migrating, and Equatorial Jets. *Journal of Atmospheric Sciences*, **60**, 1270–1296.